



## Tectonics

### RESEARCH ARTICLE

10.1029/2018TC005170

#### Key Points:

- Continental arc and back-arc magmatism in eastern NE China migrated eastward over time in Cretaceous, triggered by Paleo-Pacific rollback
- Intermediate-felsic calc-alkaline volcanics and plutons and their alkaline lamprophyre dikes mark the arc front and its termination
- Transition from Early Cretaceous intraplate extension to Late Cretaceous compression was triggered by subduction of an increasingly younger slab

#### Supporting Information:

- Supporting Information S1

#### Correspondence to:

M. Sun,  
smd@zju.edu.cn

#### Citation:

Sun, M., Chen, H., Milan, L. A., Wilde, S. A., Jourdan, F., & Xu, Y. (2018). Continental arc and back-arc migration in eastern NE China: New constraints on Cretaceous Paleo-Pacific subduction and rollback. *Tectonics*, 37, 3893–3915. <https://doi.org/10.1029/2018TC005170>


Received 20 JUN 2018

Accepted 12 SEP 2018

Accepted article online 17 SEP 2018

Published online 23 OCT 2018

# Continental Arc and Back-Arc Migration in Eastern NE China: New Constraints on Cretaceous Paleo-Pacific Subduction and Rollback

Mingdao Sun<sup>1,2,3,4</sup> , Hanlin Chen<sup>2</sup> , Luke A. Milan<sup>4</sup> , Simon A. Wilde<sup>3</sup> , Fred Jourdan<sup>3</sup> , and Yigang Xu<sup>1</sup> 

<sup>1</sup>State Key Laboratory of Isotope Geochemistry, Guangzhou Institute of Geochemistry, Chinese Academy of Science, Guangzhou, China, <sup>2</sup>Department of Earth Science, Zhejiang University, Hangzhou, China, <sup>3</sup>Department of Applied Geology, Curtin University, Perth, Western Australia, Australia, <sup>4</sup>Department of Earth Science, University of New England, Armidale, New South Wales, Australia

**Abstract** Tectonic evolution models for the Cretaceous Russia Sikhote-Alin and eastern NE China continental margin and interior remain controversial. To understand the magmatic evolution over time and assess regional geodynamic processes, we sampled a diverse array of igneous rocks and employed zircon U-Pb dating, hornblende and plagioclase <sup>40</sup>Ar-<sup>39</sup>Ar dating, whole-rock major and trace element analysis, and <sup>87</sup>Sr/<sup>86</sup>Sr and <sup>143</sup>Nd/<sup>144</sup>Nd isotopic analysis. The west Sikhote-Alin Pikeshan Formation volcanics and associated granites occurred at a peak of ~118 Ma and are hosted by the Triassic-Jurassic accretionary complex. Their whole rock geochemistry shows that SiO<sub>2</sub> increased in a linear trend, Eu/Eu\* values decreased from 0.91 to 0.38, and  $\epsilon_{\text{Nd}}(t)$  values decreased from +0.6 to -2.9, indicating magma mixing of a juvenile mantle wedge source and continental crust, consistent with a continental arc. The arc thickened over time with a felsic dike hosted in the Pikeshan granites showing depletion in heavy rare earth elements. The termination of the arc front is documented by the ~107-Ma intermediate lamprophyre and felsic dikes with  $\epsilon_{\text{Nd}}(t)$  values of +4.5 to +1.1, indicating an increased mantle contribution over time. Lithospheric extension of the Jiamusi Block to the west occurred at ~100 Ma, characterized by bimodal volcanism and composite dike emplacement, suggestive of asthenosphere upwelling. Based on the spatial and temporal distribution of these igneous rocks, the continental arc and intraplate magmatism migrated eastward contemporaneously. We favor a model invoking rollback of the subducting Paleo-Pacific slab affecting a long-lived continental arc.

## 1. Introduction

Cretaceous continental arcs are considered to have formed a continuous circum-Paleo-Pacific tectonic belt, from the North and South American Cordilleras to eastern Asia (Kirsch et al., 2016, and reference therein; Jiang & Lee, 2017). In eastern Australia, Early Cretaceous magmatism was thought to be related to the breakup of East Gondwana (Bryan et al., 1997; Ewart et al., 1992) but is recognized as continental arcs and retro-arc foreland basins formed by Paleo-Pacific subduction (Milan et al., 2016, 2017; Rey, 2013). Estimations of the global length of continental arc chains in the Cretaceous by Cao et al. (2017) do not take into account the eastern Australia arc, adding possibly ~25% more than previously estimated, making it already the longest arc since at least 750 Ma. The Cretaceous circum-Paleo-Pacific continental arc almost encircled all global continents, leaving only a gap where the Paleo-Pacific and Neo-Tethys Oceans converged, forming the basement of the present Philippines archipelago (Deng et al., 2015; Metcalfe, 2009). This Cretaceous continental arc flare-up influenced the tectonic evolution of the circum-Pacific continents and was the main driving force for magmatism, exhumation, and sedimentation at both the plate margins and the continental interiors (Paterson et al., 2004; Pearson et al., 2017). It was also a principal driver of greenhouse climates, due to the massive release of greenhouse gases by arc volcanism (McKenzie et al., 2016). Long-lived icehouse conditions followed in the Cenozoic due to decreased CO<sub>2</sub> outputs and an increase in regional weathering efficiency of the remnant arc topography (Lee et al., 2015).

In the Early Cretaceous, the Russian Far East and NE China, Korea, and Japan, as well as the Chinese continental shelf, collectively constituted the eastern Asian continental margin before the opening of the marginal seas (Tang et al., 2016). The integrated continental margin was formed by Paleo-Pacific subduction

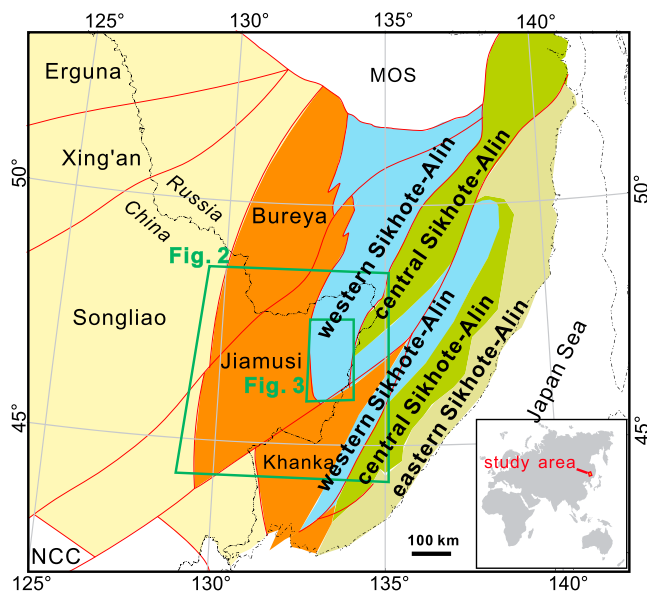


**Figure 1.** Tectonic framework of eastern NE China and Russian Primorye (after Khanchuk et al., 2016; Sun et al., 2013). The MOS and NCC are abbreviations for Mongol-Okhotsk suture and North China Craton, respectively. The locations of the maps in Figures 2 and 3 are also shown.

beneath the East Asian continent, which can be reconstructed when moving the Japanese Islands back to the Asian continental margin (Liu et al., 2017). A Late Mesozoic-Early Cenozoic magmatic belt has been proposed along the eastern margin of NE Asia (Garver et al., 2000; Xu et al., 2013; Zhao et al., 2017). Evidence for this continental arc and back-arc/retro-arc system is found in Korea (Chough & Sohn, 2010) and South China (Li et al., 2018).

Although global reviews and regional studies accept the existence of a Late Mesozoic continental arc along the eastern margin of NE Asia, the Cretaceous tectonic evolution of the continental arc and back-arc system remains controversial. A 130–115-Ma island arc system was proposed (Markevich et al., 2007; Grebennikov et al., 2016; Khanchuk et al., 2016) based on recognition of (1) the Early Cretaceous Kema island arc in the east Sikhote-Alin and (2) by the Early Cretaceous Zhuravlevka-Amur turbidite back-arc basin. Other competing tectonic models for the Late Cretaceous include an offshore convergent boundary, distal to the Asian continental margin (e.g., Bazhenov et al., 2001), and a continent-continent collision responsible for the Late Cretaceous intraplate compression in NE China (Zhang et al., 2017).

In light of these competing tectonic models, we identified several fundamental questions that need to be carefully evaluated to find a solution. First, did a continental arc develop on the Paleo-Pacific margin of East Asia in the Cretaceous? Second, if there was a continental arc, when did the arc and back-arc system form, and where was the volcanic front? Third, what are the petrological and geochemical differences between the arc and back-arc magmatism? Lastly, did the arc and back-arc system migrate over time and what are the implications for Paleo-Pacific subduction?

In this paper, we studied the geochronology and geochemistry of the Early to Middle Cretaceous igneous rocks in the Wandashan Orogen (Chinese part of the Sikhote-Alin Orogen) and the Jiamusi Block to the west. These results enable us to review the spatial and temporal migration and differences between the arc and intraplate magmatism, to better understand the tectonic evolution of the continental arc and back-arc system in the Northwest Paleo-Pacific subduction belt.

## 2. Geological Background

The tectonic units in the study area from west to east are the Songliao and Jiamusi blocks and the Sikhote-Alin Orogen (Figure 1).

The Songliao Block has a basement with affinities to both Mongolia and NE Gondwana, evidenced by the inherited zircon age spectra in Cenozoic basalts ranging from ~550 Ma and ~0.8, 1.8, and 2.5 Ga (Pan et al., 2014). It is mainly covered by the Cretaceous Songliao Basin (Feng et al., 2010) with terrestrial clastic sedimentary rocks and also Yingcheng Formation volcanic rocks (Zhang et al., 2011). The Zhangguangcai-Lesser Xing'an Range (ZGC-LXR) is a south-north trending batholith belt (Figure 2) located at the east margin of the Songliao Block (Guo et al., 2015; Ge et al., 2017; Qin et al., 2016; Wang et al., 2017; Yu et al., 2012).

The Jiamusi Block consists mainly of Pan-African metamorphic basement rocks (Mashan Complex) and minor Neoproterozoic metamorphosed igneous rocks (Wilde et al., 2003; Yang et al., 2018). It also hosts Early Cretaceous terrestrial-facies basins, with the Chengzihe, Muling, and Houshigou Formation sedimentary rocks and the overlying Songmuhe Formation volcanic rocks (Sun et al., 2015). The Heilongjiang Complex has mid-oceanic ridge basalt (MORB)- and oceanic island basalt (OIB)-type blueschist-facies ultramafic-mafic schists and marks the suture between the Songliao and Jiamusi blocks (Figure 2; Dong et al., 2018; Ge et al., 2017; Li et al., 2009; Wu et al., 2007; Zhou et al., 2009, 2010).

The Sikhote-Alin Orogen records the long subduction and accretion history of the Paleo-Pacific (Khanchuk et al., 2016) and can be subdivided into western, central, and eastern parts (Cushman & Wallin, 2000; Filippov & Kemkin, 2005; Grebennikov & Popov, 2014). The west Sikhote-Alin, from north

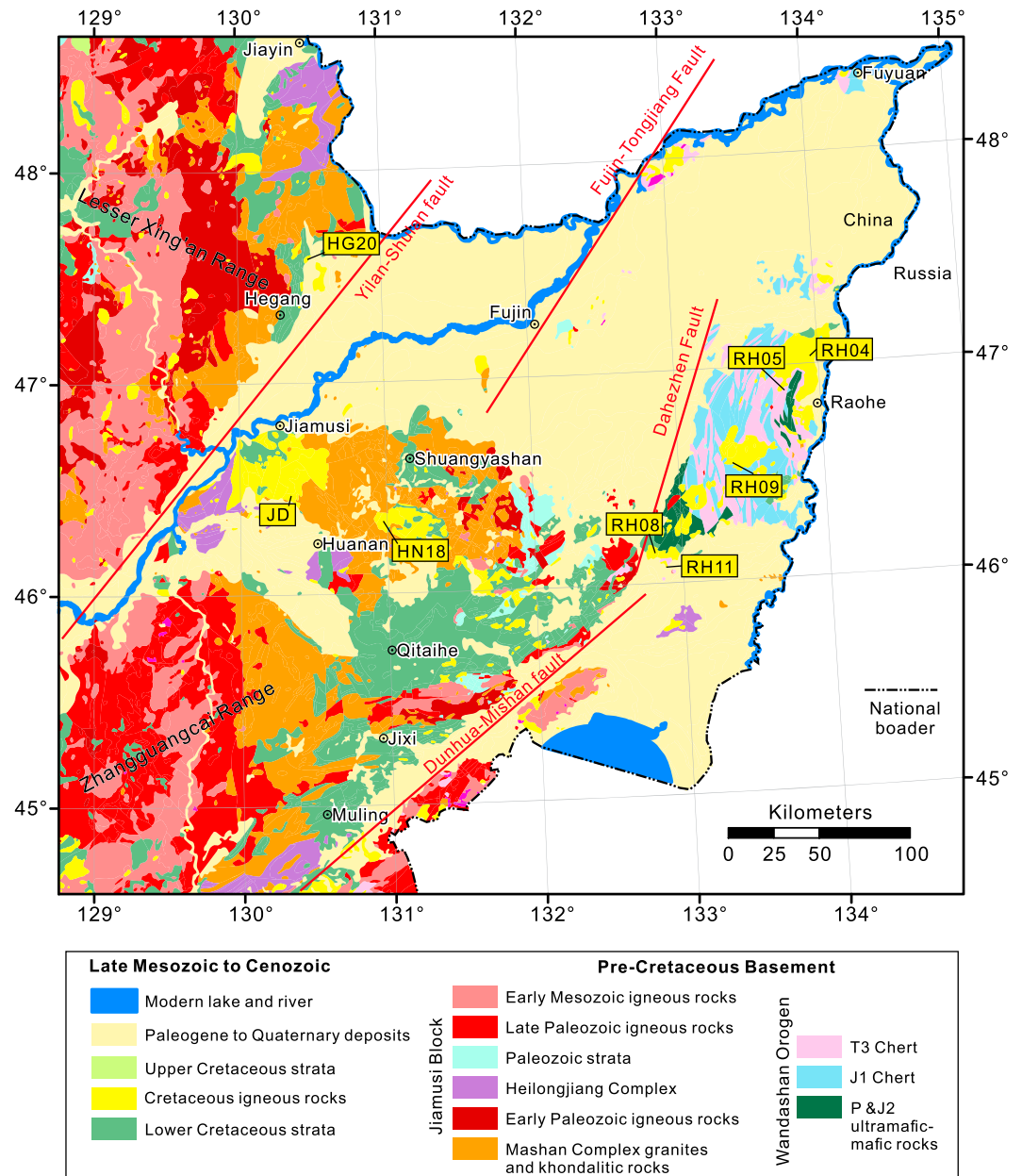


**Figure 2.** Geological map of eastern NE China (after 1:500,000 digital geological map Huang & Li, 2001), showing outcrop locations. The blank part is beyond the national borders.

to south, is composed of the Badzhai, Khabarovsk, Nadanhada-Bikin, and Samarka terranes, separated by lateral faults. They contain accreted Permian island arc suites, Triassic to Jurassic marine strata, and OIB-type igneous rocks. There are also Early Cretaceous volcanics and I-type and S-type granitoids (Kruk et al., 2014). The central Sikhote-Alin is mostly composed of the deformed Zhuravlevka turbidite basin, minor mid-Cretaceous granitoids rocks, and the Kiselevka-Manoma Hauterivian-Early Albian accretionary prism (Markevich et al., 2007). The eastern Sikhote-Alin mainly consists of Late Cretaceous to Paleogene ignimbrites and granitoids (Grebennikov & Popov, 2014; Tang et al., 2016). There are also scattered exposures of Early Cretaceous basaltic rocks (Bazhenov et al., 2001; Malinovsky et al., 2005, 2008).

The Wandashan Orogen (Sun et al., 2015) is the Chinese part of the western Sikhote-Alin Orogen. It has the same rock assemblage and is also similar to the Mino Complex in SW Japan. Early Cretaceous magmatism in

the Wandashan Orogen is marked by the Pikeshan Formation volcanics and the Hamatong, Hamahe, and Taipingcun plutons (Figure 3).

### 3. Field Geology and Petrography

#### 3.1. Pikeshan Formation (K<sub>1</sub>pk) Andesite-Rhyolite (RH08, RH09, and RH11)

The Pikeshan Formation intermediate-felsic volcanic rocks represent the major Early Cretaceous record in the Wandashan Orogen. Three outcrops were selected for sample collection (Figure 3).

Sample site RH11 (46°5′45″N, 133°51′14″E) is located in a quarry to the east of the Jian-Hu Freeway. It shows the Pikeshan Formation andesite and andesitic volcanic breccia (Figures S1a and S1b in the supporting information) layers overlying the retro-arc clastic rocks that dip 180/30° (dip direction and dip). Most lithic fragments in the volcanic breccia are andesite. There are also minor ultramafic rock and chert xenoliths (<5%), most likely being captured from the underlying accreted ophiolitic complex. The andesite is dark gray to black, characterized by clinopyroxene and plagioclase phenocrysts (Figure S1a). Seven andesite samples RH11-3 to RH11-9 were collected.

Sample site RH08 (46°9′0″N, 132°49′42″E) is located at the eastern side of the Jian-Hu Freeway from Hulin city to Jiansanjia city, near Dahezhen. The road section extends over a length of 50 m. The volcanic layer here has dark purple to brown porphyritic and gray-yellow porphyritic rhyolite. The phenocrysts are quartz and plagioclase, most of which are about 0.5 mm in size (Figure S1c). The orientation of the volcanic layer is 163°/39°. Seven samples were selected 5 m apart from top to bottom of the section. Samples RH08-1, RH08-2, and RH08-3 are dark purple rhyolite, whereas samples RH08-4, RH08-5, RH08-6, and RH08-7 are gray and yellow rhyolite.

Sample site RH09 lies at the southern foothills of Shending Peak (46°33′15″N, 133°26′12″E), which is a dome-shaped magmatic complex intruding the accreted Late Triassic to Early Jurassic Raohe Complex. The rhyolite is pale yellow, fine-grained and massive, with a felsophytic texture. Five rhyolite samples (RH09-1 to RH09-5) were collected from the outcrop.

#### 3.2. Hamahe Pluton and Dikes (RH04 and RH05)

The Hamahe pluton is located to the northeast of Shending Peak (Figure 3). It intrudes the Triassic to Jurassic accretionary complex and mainly consists of S-type granite with quartz, muscovite, red-brown biotite, and cordierite (Cheng et al., 2006). Intermediate dikes also occur, as shown at sample sites RH04 and RH05.

Sample site RH04 (46°4′14″N, 133°54′40″E) is a roadside exposure. Outcrops of andesitic to rhyolitic porphyry dikes are hosted in medium- to coarse-grained biotite granite country rock (Figure 4a). The dikes are vertical and trend 032°. The granite is moderately altered with ubiquitous dark to rust yellow color and mainly consists of quartz, feldspar, and biotite (Figures S1d and S1e). The andesitic porphyry dike is much harder and fresher. The phenocrysts in the andesitic porphyry are mainly plagioclase and hornblende (Figure S1f). Samples RH04-1 to RH04-7 are from the granite, whereas samples RH04-11 to RH04-16, RH04-17 to RH04-23, and RH04-25, are from the andesitic porphyry. Samples RH04-8 to RH04-10 are from the rhyolitic porphyry.

Sample site RH05 (46°57′28″N, 133°48′44″E) is located in a quarry at the foot of the Dadingzi Hill. Here lamprophyre dikes intrude granite country rock (Figure 4b). The country rock is medium- to coarse-grained biotite granite (samples RH05-1 to RH05-7 and RH05-14). The dikes are north-south trending and consist of various rock types, including vogesite (samples RH05-15 to RH05-20; Figures S1g, S1h, and S1i), camptonite (samples RH05-8 to RH05-13; Figures S1j and S1k), and sannaite (samples RH05-21 to RH05-24). Vogesite is a calc-alkaline hornblende-pyroxene lamprophyre; camptonite is an alkaline kaersutite lamprophyre with more plagioclase in the groundmass; sannaite is an alkaline kaersutite lamprophyre with more alkaline feldspar in the groundmass (Gill, 2010). The vogesite is black in hand specimen due to the abundance in hornblende and pyroxene phenocrysts. The camptonite has a light blue weathered surface. The sannaite dike is dark red due to abundant alkaline feldspar in the groundmass. The hornblende crystals in the vogesite with green margin and brown core (Figure S1g) and brown margin and green core (Figure S1h) indicate magma mixing and rapid cooling.



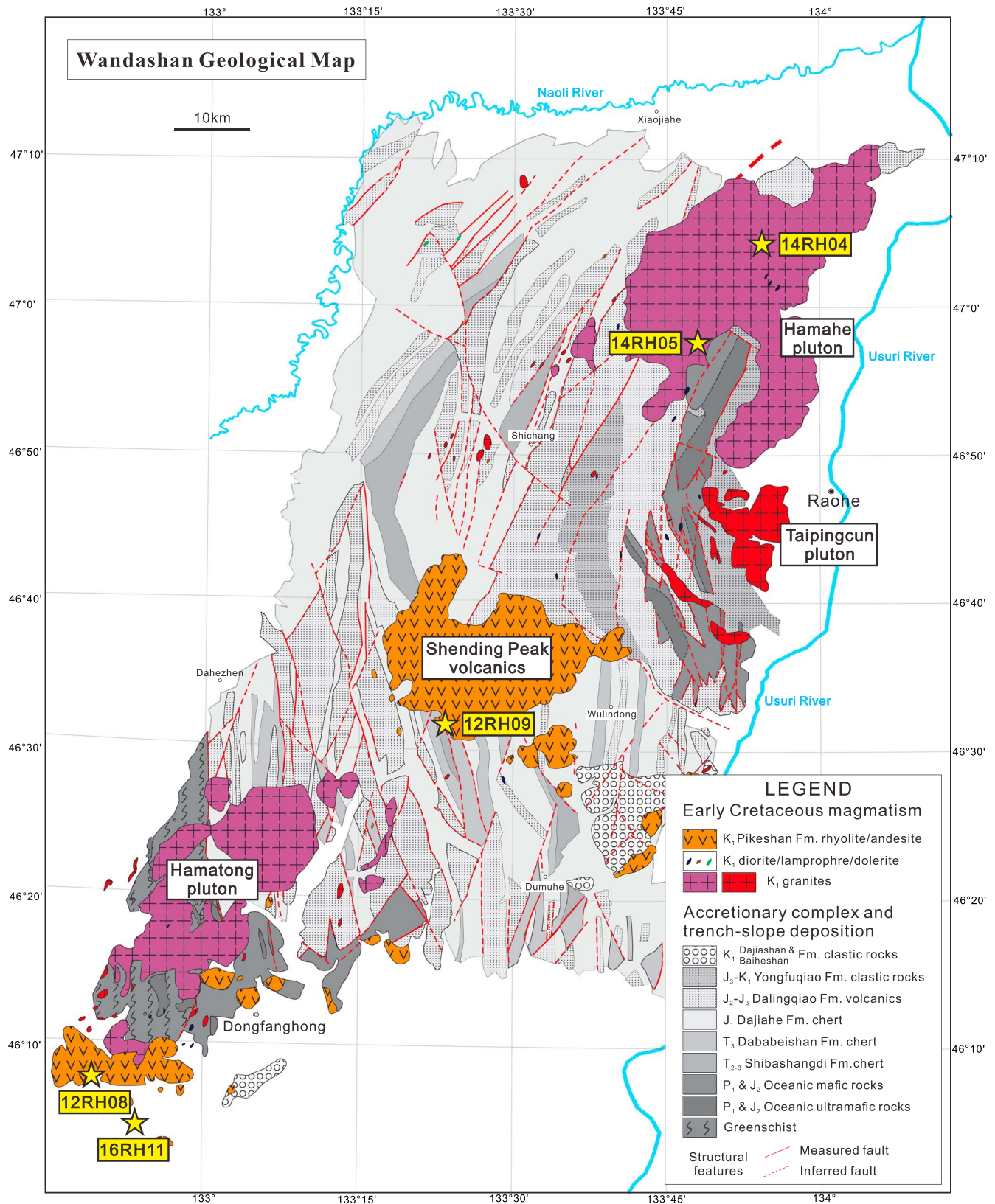


**Figure 3.** Geological map of the Wandashan Orogen showing the Hamahe, Taipingcun, and Hamatong plutons and the Shending Peak volcanics. Modified from Sun et al. (2015).

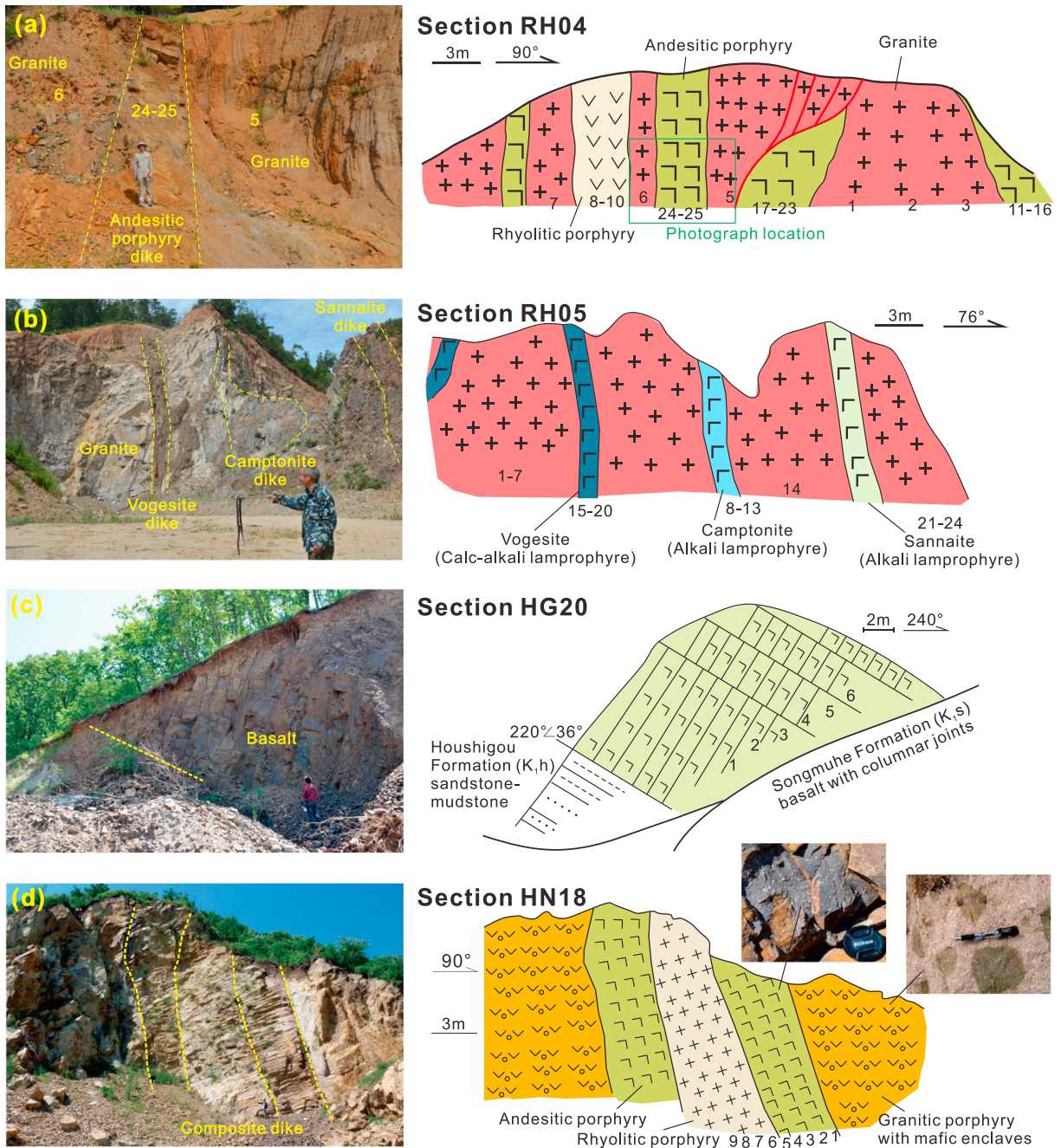


**Figure 4.** Outcrop photographs and cross sections (a) intermediate and felsic dikes in the Hamahe pluton, sample site RH04; (b) lamprophyre dikes in the Hamahe pluton, sample site RH05; (c) Songmuhe Formation basalt, sample site HG20; and (d) Huanan composite dike, sample site HN18. Photograph (a) shows only part of the section of the andesitic porphyry dike (samples 24–25) and adjacent granite. The flexural feature of the camptonite dike in the photograph (b) is caused by outcrop topography.

### 3.3. Songmuhe Formation Basalt (HG20)

The Songmuhe Formation is the uppermost Cretaceous strata in the Jiamusi Block. It conformably covers the Albian Houshigou Formation clastic rocks and has two members including the Xigemu basalt lower member and the Aoqi Ferroan (A-type) rhyolite upper member (Sun et al., 2013). Sample site HG20 (Figure 2) shows the contact between the Songmuhe and Houshigou Formations ( $47^{\circ}34'52''\text{N}$ ,  $130^{\circ}23'49''\text{E}$ ) to the northeast of Hegang city (Figure 4c). The road section extends for 30 m in length. The Songmuhe Formation basalt overlies white mudstone and sandstone of the Houshigou Formation. The columnar joints in the basalt are



perpendicular to the underlying mudstone, which dips 220/36° (dip direction and dip). The basalt is black, with a weathered brown surface, and is fine to medium grained with an intergranular texture. It consists of ~70% plagioclase, 20% augite, <5% olivine, and <5% Fe oxides (Figures S1l and S1m). Seven samples (HG20–1 to HG20–7) were collected for whole-rock geochemical analysis.

### 3.4. Huanan Composite Dike (HN18)

Composite dikes represent a unique kind of bimodal magmatism where coexisting mafic and felsic magmas occur within the same fracture system (Perring & Rock, 1991; Taylor et al., 1980) and are essentially subdivided into two types: those with a mafic interior and felsic margins (Type 1) and those with felsic interior and mafic margins (Type 2; Katzir et al., 2007; Snyder et al., 1997; Wiebe & Ulrich, 1997). The Huanan composite dike is a typical Type 2 composite dike located along the road (46°19′39″N, 130°58′23″E) halfway between Shuangyashan City and Huanan Town (Figures 2 and 4d). The road section extends over a length of 50 m and consists of an 11-m-wide composite dike, which is subvertical and trends north-south and also granitic porphyry country rock, which contains mafic microgranular enclaves (MMEs).

The Huanan composite dike has a 5-m-wide felsic interior and two 3-m-wide mafic margins (Figure 4d). Its felsic interior is pale yellow rhyolitic porphyry, which has 10% 0.2–0.5-mm quartz phenocrysts and 90% cryptocrystalline matrix (Figure S1n). The mafic margins are a black andesitic porphyry comprising 30% 1–2-mm plagioclase phenocrysts (Figure 4d) and groundmass with less quartz phenocrysts (Figure S1o). Minor occurrences of plagioclase crystals were observed in the cryptocrystalline matrix. The country rock is granitic porphyry with MMEs, again showing magma mixing. K-feldspar phenocrysts have a mode of 25% and were red colored and 2 mm in size, and the remaining 75% was a pale yellow felsophyric groundmass. The MMEs are mostly round with a diameter of 5 cm. Some enclaves are more irregular but have the same mineral composition.

Nine samples were collected from the composite dike, spanning from the margin to the interior. Samples HN18-1 to HN18-5 are andesite porphyry, and samples HN18-6 to HN18-9 are rhyolite porphyry. Samples HN14-2, HN14-4, HN14-6, HN14-8, HN14-10, and HN14-12 are from the country rock granitic porphyry; sample HN14-1 is from a mafic enclave.

## 4. Analytical Methods

### 4.1. Whole Rock Geochemistry

Rock samples were crushed to 200 mesh for whole-rock geochemical analysis. Major elements were analyzed using X-ray fluorescence spectrometry at the State Key Laboratory of Isotope Geochemistry, Guangzhou Institute of Geochemistry, Chinese Academy of Sciences (SKLIG-GIG-CAS) and the Center of Modern Analysis, Nanjing University. Trace element analyses were carried out at SKLIG-GIG-CAS, using a Finnigan Element Inductively-Coupled Plasma Mass Spectrometer (ICP-MS), and at the State Key Laboratory for Mineral Deposits Research, Nanjing University, using a PerkinElmer Elan 6000 ICP-MS. The mean relative standard deviation (RSD %) is less than 1.5%. The Sr-Nd isotopes were analyzed at the State Key Laboratory for Mineral Deposits Research, Nanjing University, using a Thermal Ionization Mass Spectrometer Finnigan Triton TI and at SKLIG-GIG-CAS using a Thermo Finnigan Neptune MC-ICP-MS. Sr isotopic ratios were normalized to an  $^{86}\text{Sr}/^{88}\text{Sr}$  ratio of 0.1194 and Nd-isotopic ratios to a  $^{146}\text{Nd}/^{144}\text{Nd}$  ratio of 0.7219. Detailed procedures follow Sun et al. (2015).

### 4.2. Zircon U-Pb Geochronology

Approximately 5–10 kg of rock were collected for each sample for zircon separation. Zircon crystals were extracted at the Langfang Geological Services Corporation, Hebei Province, China. The zircons were then mounted in epoxy resin and polished, along with standard zircons TEMORA-1 and BR266. Cathodoluminescence (CL) images were taken using a Philips XL30 Scanning Electron Microscope at Curtin University, the Institute of Geology and Geophysics of CAS, and the Beijing SHRIMP Center.

Samples HN18-1, HN18-6, RH08-1, and RH09-1 were dated using the SHRIMP ion microprobe at the John de Laeter Centre of Mass Spectrometry (JdLCMS) at Curtin University, along with zircon standard BR266 (559 Ma,  $U = 909$  ppm; Stern, 2001). Sample HN14-2 was analyzed at the Beijing SHRIMP Center, along with standard zircons SL13 and TEM-1 (Black et al., 2003) for U concentration and age calibration, respectively. The analytical

procedure was similar to that described by Williams (1998) and Wan et al. (2005). The mass resolution was ca. 5,000 at 1% peak height, and the spot size of the ion beam was 25–30  $\mu\text{m}$ . Six scans through the mass range were used for data collection. Ages and concordia diagrams were calculated using the programs SQUID 1.03 (Ludwig, 2001) and ISOPLOT 3 (Ludwig, 2003). Samples RH04-6, RH05-4, and RH05-15 were dated using the Resolution M-50 laser ablation system and Agilent 7500a ICP-MS in the Key Laboratory of Mineralogy and Metallogeny, GIG-CAS, corrected by National Institute of Standards and Technology (NIST) SRM610 glass and 91500 standard zircons and monitored by TEM-1 standard zircon. The U-Pb age diagrams were drawn using ISOPLOT 4.1 (<http://www.bgc.org/>) with ellipses error of 1-sigma.

### 4.3. $^{40}\text{Ar}$ - $^{39}\text{Ar}$ Dating

Plagioclases and amphiboles were separated from the 150–215- $\mu\text{m}$  fractions using a Frantz isodynamic magnetic separator, handpicked grain by grain under the binocular stereomicroscope, further leached using diluted HF (2 N) for 5 min, thoroughly rinsed in distilled water, and loaded into separate aluminum discs. The discs were irradiated for 40 hr during two separate irradiations, alongside Fish Canyon sanidine standards (Jourdan & Renne, 2007), for which the age of 28.294 Ma ( $\pm 0.13\%$ ) was used (Renne et al., 2011). The discs were Cd-shielded (to minimize undesirable nuclear interference reactions) and irradiated in the Oregon State University nuclear reactor (USA) in the central position. The mean  $J$  values computed from standard grains within the small pits yielded values of 0.008215 ( $\pm 0.19\%$ ) and 0.0105508 ( $\pm 0.04\%$ ) for the plagioclase and hornblende samples, respectively. Mass discrimination was monitored regularly through the analysis using an automated air pipette and provided mean values of 1.006264 ( $\pm 0.36\%$ ) and 0.992296 ( $\pm 0.04\%$ ) per Dalton (atomic mass unit) for plagioclase and hornblende, respectively, relative to an air ratio of  $298.56 \pm 0.31$  (Lee et al., 2006). The correction factors for interfering isotopes were ( $^{39}\text{Ar}/^{37}\text{Ar}$ ) Ca =  $6.95 \times 10^{-4}$  ( $\pm 1.3\%$ ), ( $^{36}\text{Ar}/^{37}\text{Ar}$ ) Ca =  $2.65 \times 10^{-4}$  ( $\pm 0.84\%$ ), and ( $^{40}\text{Ar}/^{39}\text{Ar}$ ) K =  $7.30 \times 10^{-4}$  ( $\pm 12.4\%$ ; Renne et al., 2013).

The  $^{40}\text{Ar}/^{39}\text{Ar}$  analyses were performed at the Western Australian Argon Isotope Facility at Curtin University. The plagioclase crystal population was step-heated using a double-vacuum high-frequency Pond Engineering© furnace. The gas was purified in a stainless steel extraction line using two AP10 and one GP50 SAES getters and a liquid nitrogen condensation trap. Ar isotopes were measured in the static mode using a MAP 215-50 mass spectrometer (resolution of  $\sim 400$ ; sensitivity of  $4 \times 10^{-14}$  mol/V) with a Balzers SEV 217 electron multiplier mostly using 9 to 10 cycles of peak hopping. The data acquisition was performed with the Argus program written by M. O. McWilliams and ran under a LabView environment. The hornblende crystal population was step-heated using a continuous 100 W PhotonMachine© CO<sub>2</sub> (IR, 10.4- $\mu\text{m}$ ) laser fired on the crystals for 60 s. The gas was purified in an extra low-volume stainless steel extraction line of 240 cc and using one SAES AP10 and one GP50 getter. Ar isotopes were measured in the static mode using a low volume (600 cc) ARGUS VI mass spectrometer from Thermofisher© set with a permanent resolution of  $\sim 200$ . Measurements were carried out in the multicollection mode using four faradays to measure mass 40 to 37 and a 0-background compact discrete dynode ion counter to measure mass 36. We measured the relative abundance of each mass simultaneously using 10 cycles of peak-hopping and 33 s of integration time for each mass. Detectors were calibrated to each other electronically and using Air shot beam signals.

The raw data were processed using the ArArCALC software (Koppers, 2002), and the ages have been calculated using the decay constants recommended by Renne et al. (2011). Our criteria for the determination of plateau are as follows: plateaus must include at least 70% of  $^{39}\text{Ar}$ . The plateau should be distributed over a minimum of three consecutive steps agreeing at 95% confidence level and satisfying a probability of fit (P) of at least 0.05. Plateau ages are given at the  $2\sigma$  level and are calculated using the mean of all the plateau steps, each weighted by the inverse variance of their individual analytical error. Age uncertainties include all sources of errors and have been calculated following Renne et al. (2010).

## 5. Results

### 5.1. Pikeshan Formation (K<sub>1</sub>pk) Andesite-Rhyolite (RH08, RH09, and RH11)

#### 5.1.1. Age of the Pikeshan Formation

The zircon SHRIMP results are presented in Table S1a. The zircons are about 80–250  $\mu\text{m}$  in diameter and transparent, showing oscillatory zonation as typical magmatic zircons in CL images. Eighteen zircon grains were analyzed from rhyolite sample RH08-1. The U and Th concentrations range from 89 to 1,135 ppm and



from 27 to 498 ppm, respectively, with Th/U ratios ranging from 0.30 to 0.83. One grain with an age of  $298 \pm 5$  Ma is considered to be a xenocryst. Six other grains were excluded from the calculations because of discordance greater than 15%. The remaining 11 analyses record a weighted mean  $^{206}\text{Pb}/^{238}\text{U}$  age of  $118 \pm 2$  Ma (MSWD = 2.3; Figure 5a). Fifteen zircon grains were analyzed from rhyolite sample RH09-1. The U and Th concentrations vary from 129 to 1,396 ppm and from 32 to 212 ppm, respectively, with Th/U ratios ranging from 0.15 to 0.65. Seven grains were excluded from the calculations because of discordance. The remaining eight analyses gave a weighted mean  $^{206}\text{Pb}/^{238}\text{U}$  age of  $118 \pm 3$  Ma (MSWD = 4.0; Figure 5b). Thus, the eruption of the Pikeshan Formation volcanics occurred in Aptian at  $\sim 118$  Ma.

### 5.1.2. Geochemical Results

The major and trace element results are listed in Table S2a. The Sr-Nd isotope results are presented in Table S3.

The Pikeshan Formation andesite samples RH11-3 to RH11-9 have  $\text{SiO}_2$  contents of 62.07 to 65.60 wt. %,  $\text{Na}_2\text{O}$  of 3.81 to 4.17 wt. %, and  $\text{K}_2\text{O}$  of 1.85 and 2.27 wt. % (Figure 6a). The rhyolite samples RH08-1 to RH08-7 and RH09-1 to RH09-5 have  $\text{SiO}_2$  contents of 69.13 to 73.75 wt. %,  $\text{Na}_2\text{O}$  of 2.69 to 4.21 wt. %, and  $\text{K}_2\text{O}$  of 1.86 to 5.09 wt. % (Figure 6a). In the MgO versus  $\text{SiO}_2$  diagram (Figure 6b), the andesite and rhyolite (combined with the adjacent granites; Cheng et al., 2006) plot along a continuous trend, most possibly indicating magma mixing processes.

The andesite samples have REE contents in the range of 88–117 ppm, with high light rare earth element (LREE)/(heavy rare earth element) HREE ratios  $[(\text{La}/\text{Yb})_N]$  of 5.4–5.7 and minor Eu anomalies ( $\text{Eu}/\text{Eu}^*$  = 0.82–0.90; Figure 7a). The primitive mantle normalized spider diagram (Figure 7b) is characterized by enriched but flat LILE (Large Ion Lithophile Element) patterns, Nb and Ta troughs with Nb/Ta ratios of 16.4–17.2, positive spikes in Pb and Sr, and troughs in P and Ti. The rhyolite samples have REE contents in the range of 98–226 ppm, with high LREE/HREE ratios  $[(\text{La}/\text{Yb})_N]$  of 9.2–20.5 and moderate Eu anomalies ( $\text{Eu}/\text{Eu}^*$  = 0.38–0.74; Figure 7a). They have enriched LILE, depletion in Ba, oblique Nb and Ta trough with Nb/Ta ratios of 11.1–13.4, the positive spike in Pb, and troughs in Sr, P, Ti, and Y in the primitive mantle normalized spider diagram (Figure 7b). The similarities and differences between the trace element results of andesite and rhyolite suggest that plagioclase fractionation also contributed to the magma compositional variation, together with magma mixing.

The Pikeshan Formation andesite has  $\epsilon_{\text{Nd}}(t)$  values of +0.44 to +0.59 and  $(^{87}\text{Sr}/^{86}\text{Sr})_i$  ratios of 0.705703 to 0.705750. The rhyolite has  $\epsilon_{\text{Nd}}(t)$  values of  $-0.15$  to  $-0.07$  and  $(^{87}\text{Sr}/^{86}\text{Sr})_i$  ratios of 0.706099 to 0.707265. The more radiogenic and scattered signatures (Figure 8a) of the rhyolite suggests heterogeneity of the continental crust. The enriched signature of the andesite, which is relatively less radiogenic than the rhyolite, suggests a mantle source, but involving magma mixing with a crustal component.

## 5.2. Hamahe Pluton and Dikes (RH04 and RH05)

### 5.2.1. Age of the Granite and Lamprophyre Dikes

The U-Pb ages of zircons from two granite and one lamprophyre samples were analyzed using LA ICP-MS. The  $^{40}\text{Ar}$ - $^{39}\text{Ar}$  age of hornblende from lamprophyre was also determined. The results are presented in Tables S1b–S1d.

About 1 mg of zircon was extracted from granite sample 14RH04-6. Zircons are commonly 250  $\mu\text{m}$  in length with aspect ratios of  $\sim 3:1$ . They are transparent and euhedral and show strong oscillatory zonation in CL images, typical of igneous zircons. A total of 25 grains were analyzed, of which 16 gave a concordia age of  $120 \pm 2$  Ma (MSWD = 0.69), and the remaining nine points ranged in age from  $\sim 130$  to  $\sim 200$  Ma, and are interpreted as xenocrystic zircon grains (Figure 5c). Granite sample 14RH05-4 yielded about 1 mg of zircon grains, which are similar in morphology and CL response to the aforementioned 14RH04-6 zircons. A total of 26 grains were analyzed, of which 18 gave a concordia age of  $118 \pm 2$  Ma (MSWD = 0.68). The remaining nine grains ranged in age from  $\sim 130$  to  $\sim 500$  Ma and are interpreted as xenocrystic zircons (Figures 5d and 5e). Therefore, the granite of the Hamahe Pluton was emplaced synchronously with the Pikeshan Formation volcanics.

$^{40}\text{Ar}$ - $^{39}\text{Ar}$  geochronological analysis was performed on hornblende grains from vogesite sample 14RH05-15, which yield a plateau age of  $106.7 \pm 0.2$  Ma (MSWD = 0.6;  $P = 0.91$ ; Figure 5f), indicating the emplacement age of the dike. Approximately 1,000 grains of zircon were also obtained from vogesite sample 14RH05-15. The zircons are about 150  $\mu\text{m}$  in diameter and transparent, showing strong oscillatory zonation (Figure 5g). A

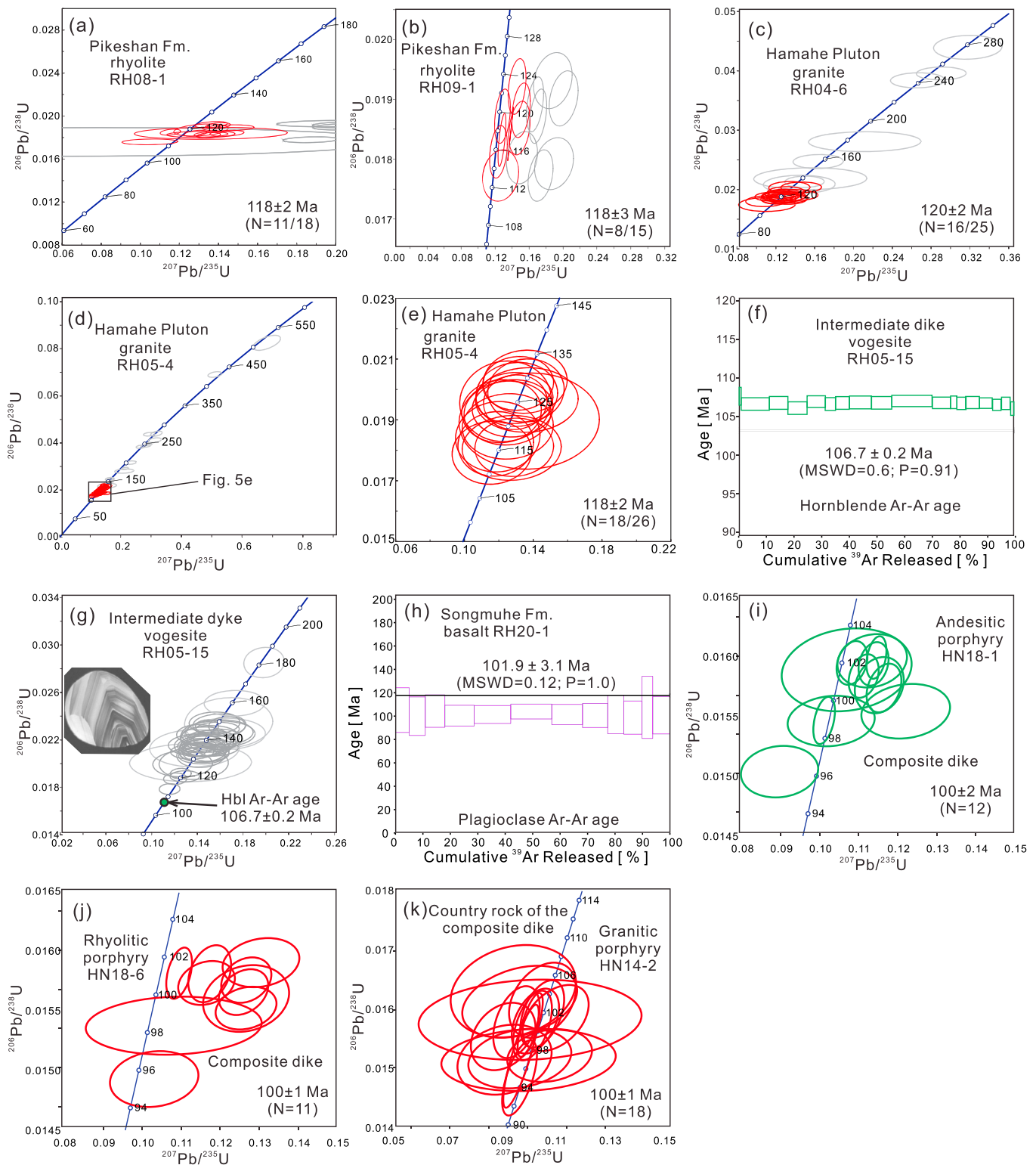


**Figure 5.** Zircon concordia diagrams and  $^{40}\text{Ar}$ - $^{39}\text{Ar}$  plateau diagrams. (a) Zircons from Pikeshan Formation rhyolite, sample RH08-1; (b) zircons of Pikeshan Formation rhyolite, sample RH09-1; (c) zircons from Hamahe pluton, sample RH04-6; (d) zircons from Hamahe pluton, sample RH05-4 (large scale showing xenocrystic zircons); (e) zircons from Hamahe pluton, sample RH05-4 (small scale showing the zircons using for calculating the emplacement age); (f) hornblende  $^{40}\text{Ar}$ - $^{39}\text{Ar}$  plateau for vogesite dike, sample RH05-15; (g) zircons from vogesite dike, sample RH05-15; (h) plagioclase  $^{40}\text{Ar}$ - $^{39}\text{Ar}$  plateau for basalt, sample RH20-1; (i) zircons from andesite porphyry of composite dike, sample HN18-1; (j) zircons from rhyolite porphyry of composite dike, sample HN18-6; (k) zircons from the granite porphyry country rock of the composite dike, sample HN14-2.

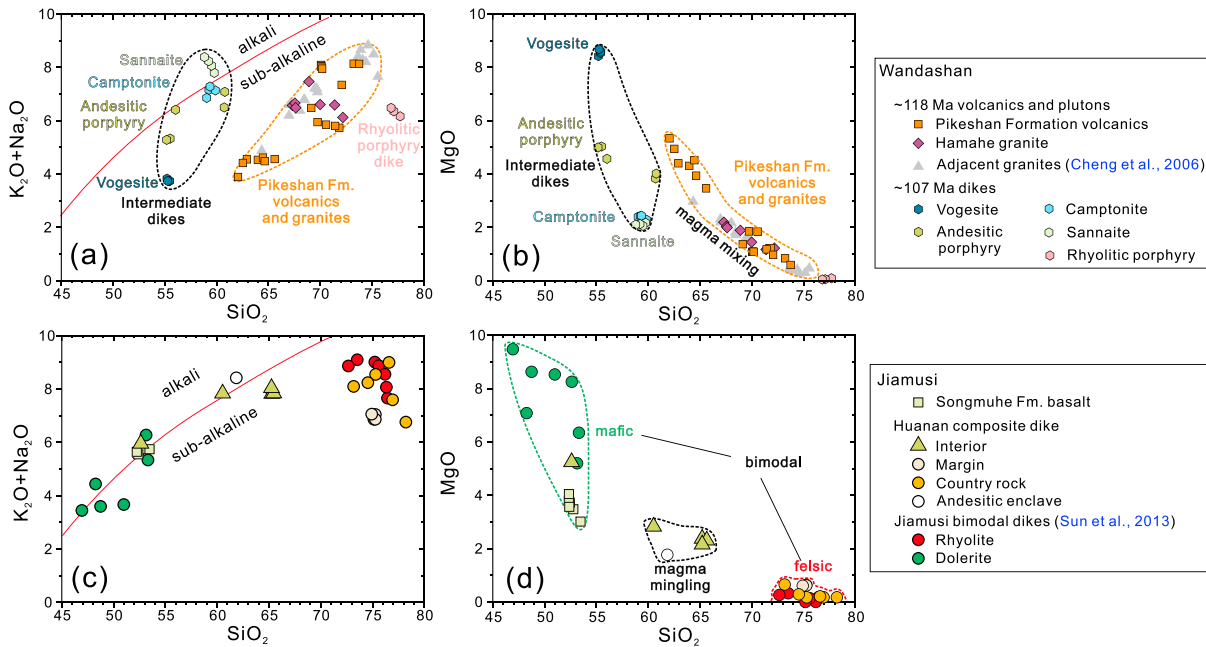


**Figure 6.** Major element diagrams (a)  $\text{Na}_2\text{O} + \text{K}_2\text{O}$  versus  $\text{SiO}_2$  plot showing the Wandashan samples; (b)  $\text{MgO}$  versus  $\text{SiO}_2$  plot showing the Wandashan samples; (c)  $\text{Na}_2\text{O} + \text{K}_2\text{O}$  versus  $\text{SiO}_2$  plot showing the Jiamusi samples; (d)  $\text{MgO}$  versus  $\text{SiO}_2$  plot showing the Jiamusi samples.

total of 50 grains were analyzed, with 41 concordant ages ranging from  $114 \pm 2$  to  $150 \pm 4$  Ma and six scattered ages ranging from  $158 \pm 7$  to  $683 \pm 7$  Ma. All zircon ages are older than the  $106.7 \pm 0.2$  Ma  $^{40}\text{Ar}$ - $^{39}\text{Ar}$  age of the hornblende suggesting that the zircons crystallized earlier than the emplacement and cooling of the lamprophyre dike and were xenocrysts originating from the continental arc crust and previous magmatic episodes.

### 5.2.2. Geochemical Results

A total of 7 granite country rock samples and 20 dike samples were analyzed. The major and trace element results are presented in Table S2b. The Sr-Nd isotope results are presented in Table S3.

The granite country rock has similar geochemical signatures to the Pikeshan Formation rhyolite. The country rock has an  $\text{SiO}_2$  content of 67.31 to 72.19 wt. %,  $\text{Na}_2\text{O}$  of 3.36 to 3.90 wt. %, and  $\text{K}_2\text{O}$  of 2.69 to 3.56 wt. %. In the REE diagram, it shows enrichment of LREE and a flat distribution pattern of HREE, depletion of Eu with  $\text{Eu}/\text{Eu}^*$  of 0.56 to 0.70 (Figure 7a). In the spider diagram, it shows enrichment of LILE, troughs in Nb, Ta, Sr, P, and Ti, and positive spikes in Pb (Figure 7b). The trace and rare element features thus suggest a continental crustal source and also the influence of plagioclase fractionation. The granite pluton has an initial  $^{87}\text{Sr}/^{86}\text{Sr}$  ratio of 0.706830 to 0.707042 and  $\epsilon_{\text{Nd}}(t)$  values of  $-2.90$  to  $-2.08$  ( $t = 118$  Ma), again indicating a source from the continental crust.

The dikes intruded in the Hamahe granite are dominated by intermediate rocks. They have significantly different geochemical characteristics from the Aptian Pikeshan volcanics and Hamahe granite, indicating various magma sources.

The rhyolitic porphyry dike (sample site RH04) has high  $\text{SiO}_2$  (76.83 to 77.71 wt. %) and low  $\text{MgO}$  (0.04–0.07 wt. %) contents and moderate  $\text{K}_2\text{O}$  (2.44–2.51 wt. %) and  $\text{Na}_2\text{O}$  (3.55–3.82 wt. %) contents. It has enrichment in LREE but ultradepletion in HREE, with  $(\text{La}/\text{Yb})_{\text{N}}$  of 202–444 (Figure 7c). In the spider diagram (Figure 7d), the rhyolitic dike shows a peak in Pb and troughs in Sr, P, and Ti. The ultradepletion in HREE likely indicates a deep source with garnet in the residue. The andesitic porphyry dikes (sample site RH04) have 55.17 to 60.79 wt. %  $\text{SiO}_2$ , 2.67 to 4.04 wt. %  $\text{Na}_2\text{O}$ , 2.60–3.04 wt. %  $\text{K}_2\text{O}$ , moderate  $\text{Mg}\#$  of 53–55, and no Eu anomalies with  $\text{Eu}/\text{Eu}^*$  of 0.94–1.04 (Figure 7c). In the spider diagram (Figure 7d), the andesitic porphyry is characterized by enrichment of LILE Rb, Ba, and K, and LREE and also has peaks of Pb and Sr and troughs in Th, U, Nb, Ta, and Ti. Samples RH04-17 to 19 that are relatively more mafic have lower LREEs and depletion in Th, Zr, and Hf, indicating less contamination from the granitic crust.

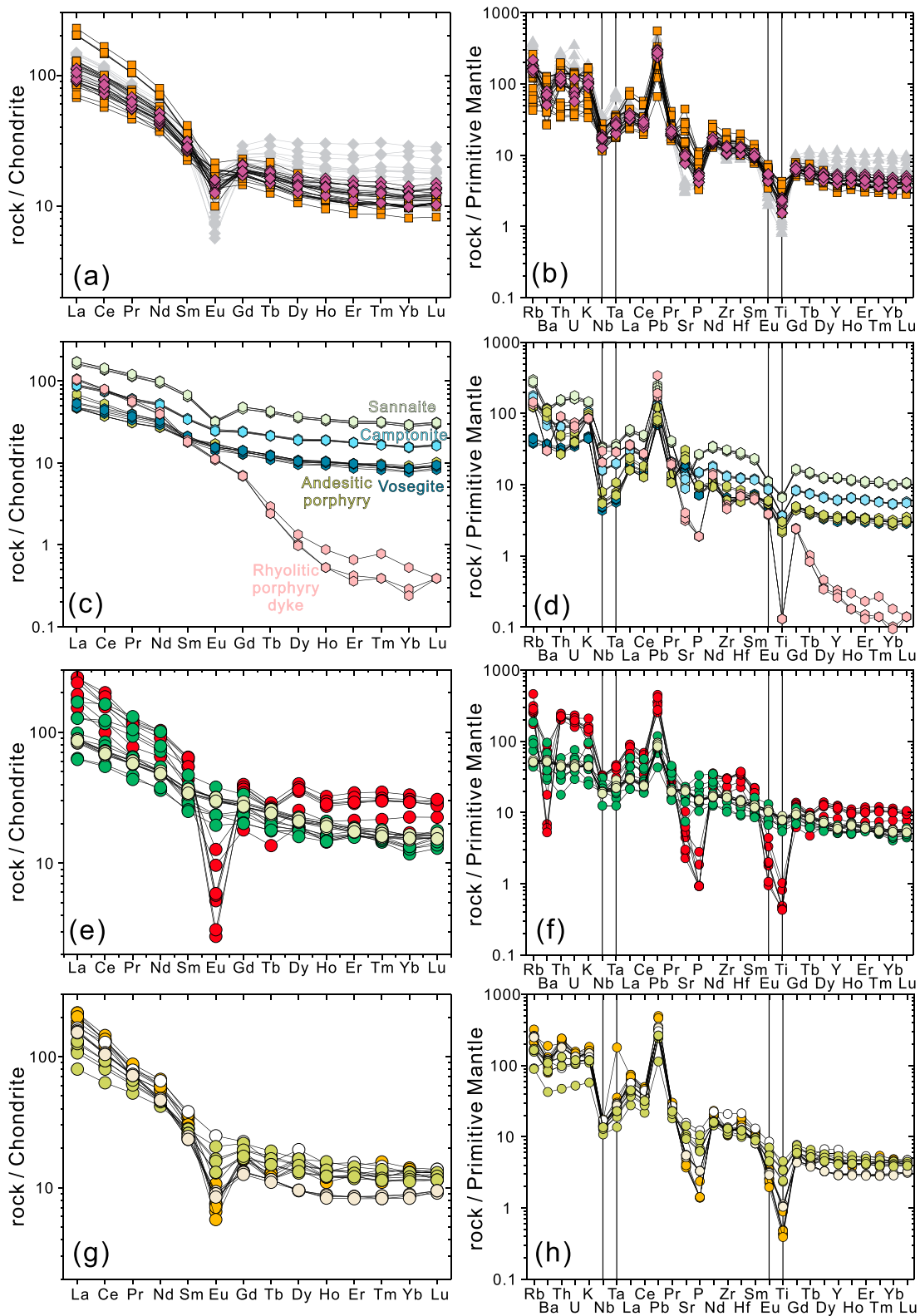


**Figure 7.** Chondrite-normalized REE diagrams and primitive mantle-normalized spider diagrams for the (a, b) Pikeshan Formation volcanics (in yellow), Hamahe granite (in purple), and associated plutons (in gray, data from Cheng et al., 2006); (c, d) the intermediate to felsic dikes; (e, f) the Songmuhe Formation basalt (light green) and bimodal dikes (in red and green; Sun et al., 2013); and (g, h) the Huanan composite dike (chondrite and primitive mantle normalization values after McDonough and Sun, 1995).



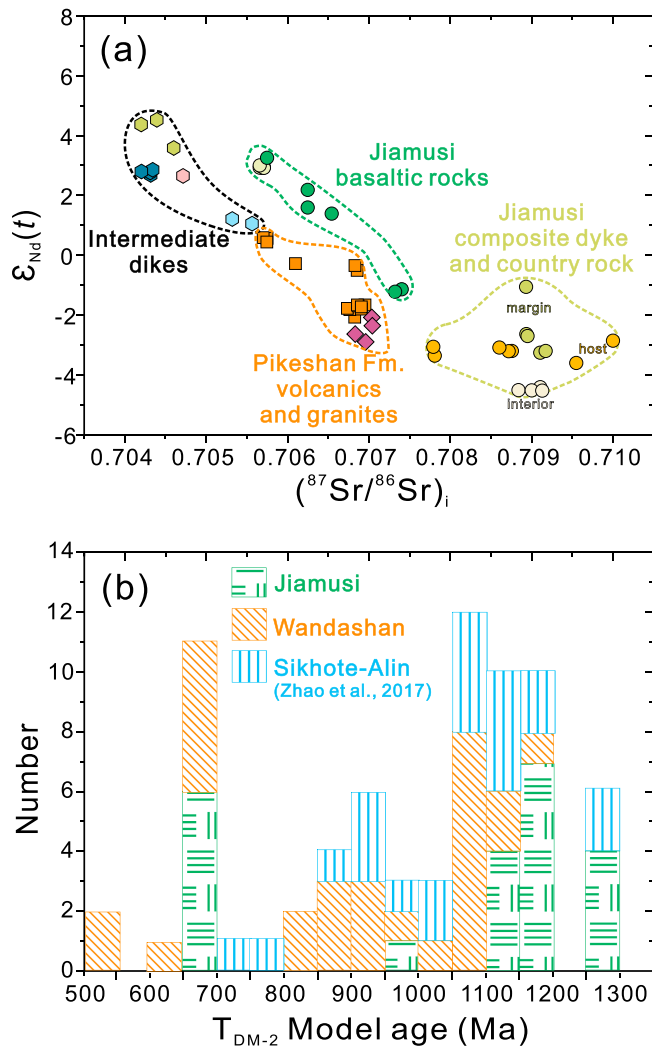


**Figure 8.** (a) The  $\epsilon_{\text{Nd}}(t)$  versus initial  $^{87}\text{Sr}/^{86}\text{Sr}$  diagram for the Jiamusi and Wandashan Cretaceous igneous rocks, showing that the Jiamusi magmatic rocks are systematically more enriched in  $^{87}\text{Sr}/^{86}\text{Sr}$  than the Pikeshan volcanics and granites and associated intermediate dikes. (b) Histogram distribution diagram of the two-stage Nd model age ( $T_{\text{DM}2}$ ).

The vogesite dike (sample site RH05) has 55.21–55.44 wt. %  $\text{SiO}_2$ , 2.34–2.39 wt. %  $\text{Na}_2\text{O}$ , and 1.33–1.43 wt. %  $\text{K}_2\text{O}$ . It has the highest Mg# value of 68–69 among the dikes, possibly due to the accumulation of hornblende phenocrysts. It shows a trace element pattern in the spider diagram similar with the andesitic porphyry samples RH04-17 to RH04-19, except that the enrichment of Rb, Ba, and K in the vogesite is not as significant as in the andesitic porphyry. The camptonite dike (sample site RH05) has higher  $\text{SiO}_2$  (59.04–59.87 wt. %) and alkali content (3.82–4.50 wt. %  $\text{Na}_2\text{O}$  and 2.63–3.21 wt. %  $\text{K}_2\text{O}$ ). It shows a similar trace element pattern to the vogesite but enrichment in bulk trace element content, with REE contents of 118–124 ppm, approximately twice that of the vogesite. It also exhibits depletion of Sr and more enrichment in K and Rb. The sannaite dike (section RH05) has similar  $\text{SiO}_2$  (58.81–59.76 wt. %) and  $\text{Na}_2\text{O}$  content (3.43–4.00 wt. %) as the camptonite but significantly more  $\text{K}_2\text{O}$  (4.21–4.43 wt. %). It shows a similar trace element pattern with the camptonite but enrichment in bulk trace element content, with REE content of 219–235 ppm, about twice that of the camptonite. It also has 5 times more Th and U than the camptonite (Figures 7c and 7d).

The above intermediate-felsic dikes have initial  $^{87}\text{Sr}/^{86}\text{Sr}$  ratios of 0.704110 to 0.705564 and  $\epsilon_{\text{Nd}}(t)$  values of +1.05 to +4.52. These isotopic signatures show that the dikes are isotopically more depleted than the Pikeshan volcanic rocks and Hamahe granite (Figure 8a).

### 5.3. Songmuhe Formation ( $K_1s$ ) Basalt

#### 5.3.1. Age of the Songmuhe Formation

The volcanic tuff in the Houshigou Formation below the Songmuhe Formation has a zircon U-Pb age of  $103 \pm 2$  Ma (Sun et al., 2014), whereas the dikes intruded into the Songmuhe Formation have an age of  $100 \pm 1$  Ma (Sun et al., 2013). The fresh plagioclase phenocrysts from the basalt sample RH20-1 were handpicked for  $^{40}\text{Ar}$ - $^{39}\text{Ar}$  analysis (Table S1b). The plagioclase package yielded a plateau age at  $101.9 \pm 3.1$  Ma (MSWD = 0.12,  $P = 1.0$ , Figure 5h), in agreement to the U-Pb data. Thus, the Songmuhe Formation basalt erupted in the latest Early Cretaceous, based on both contact relationships in the field and isotopic geochronology.

#### 5.3.2. Geochemical Results for the Songmuhe Formation

Major, trace, and rare earth element data for the Songmuhe Formation basalt are presented in Table S2c. The Songmuhe Formation basalt samples (HG20-1 to HG20-6) have  $\text{SiO}_2$  contents of 51.49 to 52.26 wt. %,  $\text{Na}_2\text{O}$  of 4.21 to 4.28 wt. %, and  $\text{K}_2\text{O}$  of 1.32 to 1.35 wt. % (Figure 6c). They are characterized by high  $\text{Al}_2\text{O}_3$  (17.83 to 18.96 wt. %) and low MgO (2.95–3.95 wt. %) (Figure 6d). The Mg# values of 0.42 to 0.45 suggest that the magma experienced crystal fractionation. The basalt samples have REE contents in the range of 116–122 ppm, with high LREE/HREE ratios  $[(\text{La}/\text{Yb})_{\text{N}}$  of 5.4–5.7) and no Eu anomalies ( $\text{Eu}/\text{Eu}^* = 0.98$ –1.00; Figure 7e). The primitive mantle normalized spider diagram is characterized by positive spikes in Pb and minor troughs in Nb, Ta, P, Ti, and Y, with Nb/Ta ratios of 14.1–15.0 (Figure 7f). The Sr-Nd isotope results are shown in Table S3. The isotopic data for the basalt are all essentially similar, with  $\epsilon_{\text{Nd}}(t)$  values of +2.92 to +3.00 and  $(^{87}\text{Sr}/^{86}\text{Sr})_i$  ratios  $\sim 0.7057$ . These Sr-Nd isotopic features are similar to dolerite sample JD01 of the Jiamusi bimodal dikes (Sun et al., 2013), indicating a depleted mantle source. Their high  $(^{87}\text{Sr}/^{86}\text{Sr})_i$  ratios were possibly caused by contamination by continental crust and/or subducting slab dehydration considering the arc-like trace element patterns.

Their high  $(^{87}\text{Sr}/^{86}\text{Sr})_i$  ratios were possibly caused by contamination by continental crust and/or subducting slab dehydration considering the arc-like trace element patterns.

### 5.4. Huanan Composite Dike (HN18)

#### 5.4.1. Age of the Huanan Composite Dike and Its Country Rock

Zircons from granitic porphyry sample HN14-2 are mostly 80 to 150  $\mu\text{m}$  long with about 2:1 aspect ratios. However, zircons from the andesitic porphyry sample HN18-1 and rhyolitic porphyry sample HN18-6 range

from 200 to 250  $\mu\text{m}$ ; both have about 3:1 aspect ratios. Notably, zircons from the composite dike sample HN18-1 and HN18-6 have many needle-shaped apatite inclusions. Care was taken to avoid inclusions during the analyses. The results are presented in Table S1e.

Twelve zircon grains were analyzed from andesitic porphyry sample HN18-1. The U and Th concentrations vary from 465 to 1,285 ppm and from 165 to 1233 ppm, respectively, with the Th/U ratios ranging from 0.35 to 0.96. The weighted mean  $^{206}\text{Pb}/^{238}\text{U}$  age is  $100 \pm 2$  Ma (MSWD = 2.9; Figure 5i). Twelve zircon grains were analyzed from rhyolitic porphyry sample HN18-6. One large zircon grain has an age of  $272 \pm 3$  Ma and Th/U ratio of 0.12 and is considered to be a xenocryst. The other 11 grains have U and Th concentrations varying from 272 to 1264 ppm and from 123 to 507 ppm, respectively, with the Th/U ratio ranging from 0.34 to 0.64. The 11 analyses give a weighted mean  $^{206}\text{Pb}/^{238}\text{U}$  age of  $100 \pm 1$  Ma (MSWD = 1.16; Figure 5j). Eighteen zircon grains were analyzed from granite porphyry sample HN14-2. The U and Th concentrations vary from 206 to 1,419 ppm and from 188 to 2,221 ppm, respectively, with the Th/U ratios ranging from 0.65 to 2.48. The weighted mean  $^{206}\text{Pb}/^{238}\text{U}$  age is  $100 \pm 1$  Ma (MSWD = 1.0; Figure 5k). There is no distinct age difference between the dike and country rock, suggesting that the dike was emplaced soon after the country rock granitic porphyry solidified.

#### 5.4.2. Geochemical Results

Major, trace, and rare earth element data for the andesite and rhyolite porphyry, diorite enclave, and granite porphyry from the Huanan composite dike and its country rock are presented in Table S2d. The andesite porphyry samples from the margin of the Huanan composite dike form three groups. Sample HN18-1, which is close to the country rock, has a  $\text{SiO}_2$  content of 56.97%. Sample HN18-2 has the lowest  $\text{SiO}_2$  content of 44.47%, with highest loss on ignition (LOI) of 9.02%, MgO of 4.78%, and Mg# of 0.58, representing the mafic magma with the least contamination. Samples HN18-3, HN18-4, and HN18-5 have  $\text{SiO}_2$  contents of 62.04–62.54% and LOI from 4.02 to 4.62 and were possibly contaminated by the felsic magma of the composite dike. The rhyolite porphyry samples from the interior of the Huanan composite dike (HN18-5 to HN18-9) have  $\text{SiO}_2$  contents of 72.77 to 73.23 wt. % and LOI from 2.26 to 2.42%. Four samples show uniform geochemical features, with 2.13–2.18%  $\text{Fe}_2\text{O}_3$ , 0.59–0.62% MgO, and Mg# = 0.38–0.39, consistent with them experiencing little contamination by felsic magma. The contents of  $\text{Na}_2\text{O}$  (2.45–2.51%),  $\text{K}_2\text{O}$  (4.18–4.40%), CaO (1.09–1.34%), and  $\text{Al}_2\text{O}_3$  (12.87–13.06%) give ASI values from 1.17 to 1.21, suggesting that the rhyolite porphyry has S-type granite affinities. The andesite porphyry dike samples have REE contents in the range of 103–133 ppm, with high LREE/HREE ratios  $[(\text{La}/\text{Yb})_N \text{ of } 6.2\text{--}11.7]$  and negative Eu anomalies ( $\text{Eu}/\text{Eu}^* = 0.62\text{--}0.83$ ; Figure 7g). They are rich in LILE and Pb depleted in Nb, Ta, Sr, P, and Ti (Figure 7h). The rhyolite porphyry dike samples have REE contents in the range of 142 to 146 ppm, with high LREE/HREE ratios  $[(\text{La}/\text{Yb})_N \text{ of } 17.6\text{--}18.4]$  and negative Eu anomalies ( $\text{Eu}/\text{Eu}^* = 0.49\text{--}0.52$ ; Figure 7g). They are rich in LILE and Pb depleted in Nb, Ta, Sr, P, and Ti (Figure 7h). The REE patterns of the andesite porphyry and rhyolite porphyry cross between Nd and Sm, similar to the pattern of the composite dike samples described by Stern and Voegeli (1987).

The granitic porphyry samples HN14-2, HN14-6, HN14-10, and HN14-12 from the country rock of the composite dike have  $\text{SiO}_2$  contents of 70.60 to 76.10 wt. %,  $\text{Na}_2\text{O}$  of 2.26 to 3.77 wt. %,  $\text{K}_2\text{O}$  of 3.55 to 5.16 wt. %, and LOI from 1.70 to 3.18%. They have variable Mg# (0.15–0.44) and A/CNK values (0.83–1.27) indicating that the felsic magma was possibly contaminated by basaltic material, or the granitic porphyry experienced various degrees of alteration. The diorite enclave sample HN14-1 in the granitic porphyry has a  $\text{SiO}_2$  content of 57.99 wt. %,  $\text{Na}_2\text{O}$  of 4.19 wt. %, and  $\text{K}_2\text{O}$  of 3.70 wt. %. The granitic porphyry samples have REE contents in the range of 166–199 ppm, with high LREE/HREE ratios  $[(\text{La}/\text{Yb})_N \text{ of } 12.7\text{--}15.7]$  and negative Eu anomalies ( $\text{Eu}/\text{Eu}^* = 0.26\text{--}0.42$ ; Figure 7g). In the primitive mantle normalized spider diagram, they are characterized by positive spikes in LILE but troughs in Nb, Ta, Sr, P, Eu, and Ti, with Nb/Ta ratios of 10.0 (Figure 7h). The diorite enclave has an REE content of 180 ppm and a high LREE/HREE ratio  $[(\text{La}/\text{Yb})_N = 12.8]$ , with minor negative Eu anomaly of 0.85 (Figure 7g). It is depleted in Nb, Ta, and Ti but enriched in LILE, with Nb/Ta ratios of 13.9 (Figure 7h).

The Sr-Nd isotope data for the Huanan composite dike are shown in Table S3. The andesite porphyry has  $(^{87}\text{Sr}/^{86}\text{Sr})_i$  of 0.7089–0.7091 and  $\epsilon_{\text{Nd}}(t)$  of  $-1.06$  to  $-3.26$ . Sample HN18-2 has the highest  $\epsilon_{\text{Nd}}(t)$  value of  $-1.06$ . Samples HN18-3, HN14-4, and HN14-5 have the lower  $\epsilon_{\text{Nd}}(t)$  value of  $-3$ . The rhyolite porphyry has  $(^{87}\text{Sr}/^{86}\text{Sr})_i$  of 0.7089–0.7091 and  $\epsilon_{\text{Nd}}(t)$  of  $-4.5$  (Figure 8a). The Nd isotopes show that more contamination of the andesite porphyry occurs closer to the host and composite dike interior felsic rocks. However, both

the andesite porphyry and rhyolite porphyry have similar Sr isotope ratios, reflecting that Sr is more mobile than Nd during contamination. The country rock granite porphyry has  $\varepsilon_{\text{Nd}}(t)$  values of  $-3.06$  to  $-3.60$  and  $(^{87}\text{Sr}/^{86}\text{Sr})_i$  ratios ranging from 0.707791 to 0.709550. The large range of  $(^{87}\text{Sr}/^{86}\text{Sr})_i$  ratios of the Huanan composite dyke and its country rock could be caused by high degree of alteration, when considering the high LOI values of some samples.

## 6. Discussion

### 6.1. Magma Sources and Evolution

#### 6.1.1. The ~118-Ma Arc Magmatism: Pikeshan Volcanics and Granites

The Pikeshan volcanic rocks and associated granites reveal a progressive evolutionary trend in terms of whole-rock geochemistry (Figures 6a, 6b, and 9a). The andesite is characterized by low Eu anomalies ( $\text{Eu}/\text{Eu}^* = 0.82\text{--}0.91$ ; Figure 9b), moderate MgO content (Figure 9c), and relatively depleted isotopic signatures. These rocks are likely sourced from the mantle wedge and experienced moderate differentiation and crustal contamination. The rhyolites and associated granites are magnesian (Figure 9a) and have similar trace element patterns with flat HREE (Figures 7a and 7b), Nb-Ta depletion, enrichment of LILE and LREE, and enriched isotopic signatures. Trends in major and trace elements and isotopic variations suggest magma mixing. In the  $\text{FeO}^{\text{T}}$  versus MgO diagram (Figure 9c), the Pikeshan volcanic rocks and associated granites plot a calc-alkaline trend, suggesting a continental arc origin and the arc crust thickness was likely larger than 75 km (Tang et al., 2018). When combined with the tectonic location (former accretionary complex), we suggest that the ~118 Ma Pikeshan Formation indicates a compressional continental arc volcanic front.

#### 6.1.2. The ~107-Ma Arc Front Termination: Intermediate-Felsic Dikes

The dikes that intruded into the ~118-Ma granite all trend north-south. However, they are different in lithology and geochemistry, indicating different magma sources.

The rhyolitic porphyry dikes show an extreme depletion of HREE with  $(\text{La}/\text{Yb})_{\text{N}}$  values of 202–444 and a low content of Y (0.26–0.33 ppm). This adakite-like signature is likely caused by partial melting of young oceanic crust or thickened/delaminated lower crust (Castillo, 2012; Defant & Drummond, 1990; Kolb et al., 2012). The high  $\text{SiO}_2$  content (76.8–77.7 wt. %) indicates that the source was composed of intermediate to felsic rocks, whereas low MgO content and lack of Eu anomalies ( $\text{Eu}/\text{Eu}^* = 0.96\text{--}1.00$ ) suggest that the magma was not derived from the oceanic slab or delaminated lower crust (Figure 9b). We interpret this signature to be thickened lower crust. The relatively high  $\varepsilon_{\text{Nd}}(t)$  value of +2.65 suggests that the source crust was juvenile. Thus, the felsic adakite-like melt was likely derived from the partial melting of an immature/juvenile lower crust, which was formed by accretion of trench deposits, leaving eclogite as the residual rock.

The intermediate dikes show major element variation from subalkaline (andesitic porphyry and vogesite) to alkaline (camptonite and sannaite), with similar trace element patterns and Sr-Nd isotopic values. The geochemical results suggest a strong contribution from the metasomatized mantle wedge or lithospheric mantle and various degrees of crustal contamination. They are similar to the lamprophyre dikes from Kyoto Prefecture, Japan based on geochronological and geochemical signatures (e.g., Imaoka et al., 2017; Kelemen, 1995; Tatsumi, 2001). Specifically, the vogesite has low  $\text{FeO}^{\text{T}}/\text{MgO}$  values of 0.82 to 0.86, high MgO contents of 8.13–8.41 wt. %, Mg# of ~68, and 93–107 ppm Ni, suggesting a high magnesian andesite. The subalkaline lamprophyres are commonly associated with granitoid plutons in orogenic belts, whereas alkaline lamprophyres are generally associated with syenite-gabbro or alkaline rock-carbonatite complexes in continental rift valleys and cratons (Gill, 2010). Therefore, we interpret the intermediate dikes as recording the ending of the continental arc due to extension, melting of the thickened lithospheric mantle, and lower crust.

#### 6.1.3. The ~103-Ma Extension-Related Basalt of the Jiamusi Block: Songmuhe Formation

The basalt samples have relatively high  $\text{SiO}_2$  (52.09–53.22%), high  $\text{Al}_2\text{O}_3$  (17.97–19.04%), low MgO (3.00–3.98%), and low Mg# (0.46–0.48), indicating that the magma experienced a high degree of fractionation. They plot along the 0–25-km differentiation line (Figure 9c), indicating that they are likely tholeiitic rather than calc-alkaline. The lack of Eu anomalies ( $\text{Eu}/\text{Eu}^* = 0.98\text{--}1.00$ ), the relatively flat LILE patterns, and positive  $\varepsilon_{\text{Nd}}(t)$  values (+2.9 to +3.0) suggest that crustal contamination is not significant. The relatively enriched  $\varepsilon_{\text{Nd}}(t)$  values (compare to MORB) and the arc-type trace element pattern indicate that the basalt was likely derived from a mantle source metasomatized by melting of altered basalt from the subducted

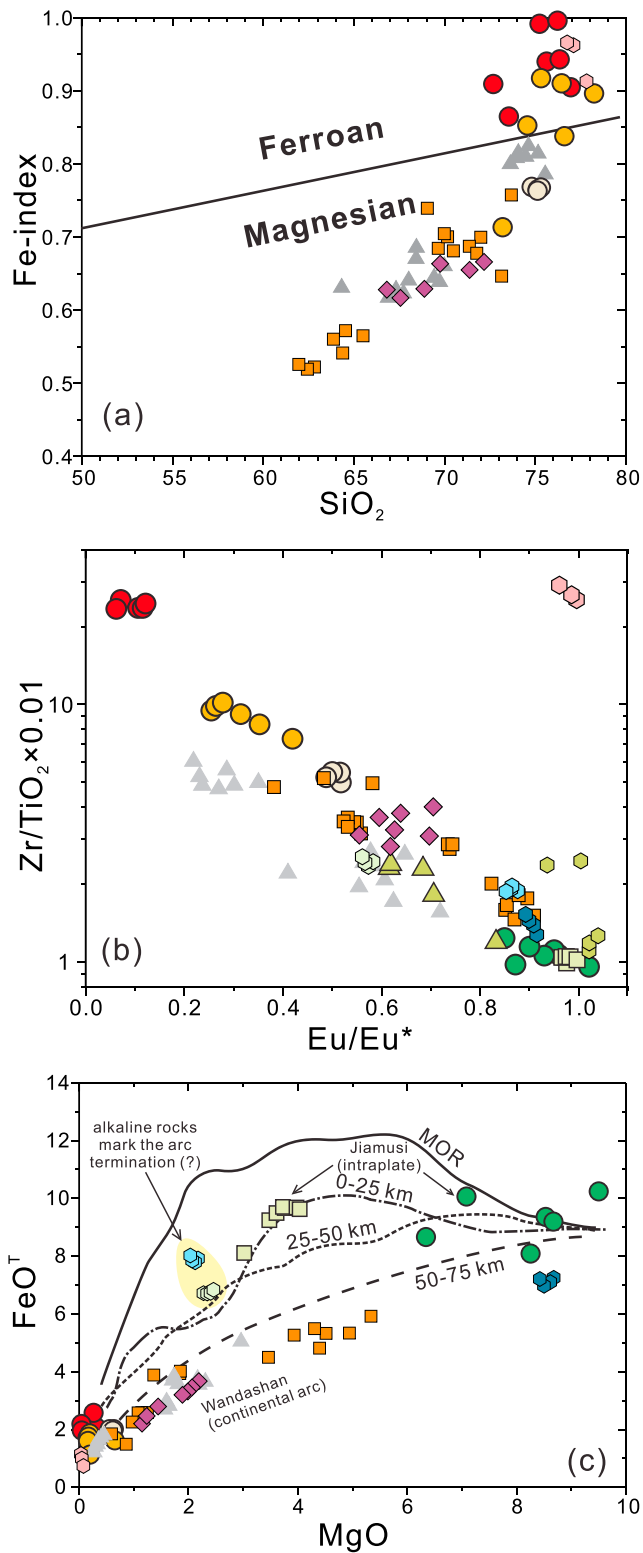


**Figure 9.** Magma origin and evolution diagrams: (a) Fe-index versus SiO<sub>2</sub> plot (Fe-index = (FeO + 0.9Fe<sub>2</sub>O<sub>3</sub>)/(FeO + 0.9Fe<sub>2</sub>O<sub>3</sub> + MgO), after Frost & Frost, 2010), (b) Zr/TiO<sub>2</sub> × 0.01 versus Eu/Eu\* diagram showing the fractionation differentiation, and (c) FeO<sup>T</sup> versus MgO diagram showing the different fractionation trend between the Jiamusi and Wandashan igneous rocks (MOR and crustal thickness lines are after Tang et al., 2018).

slab (Wang et al., 2016). Contemporaneous development of rift basins (Zhang et al., 2012) and the Songmuhe Formation basalts suggests that these rocks formed in an extensional setting.

#### 6.1.4. The ~100-Ma Extension-Related Dikes of the Jiamusi Block

The composite dike has andesitic margins and a felsic interior. The andesitic porphyry sample HN18-2 has low SiO<sub>2</sub> content (52.6 wt. %) and is close to the composition of the basaltic magma. However, the other andesitic porphyry samples have intermediate SiO<sub>2</sub> contents (60.5 to 65.5 wt. %) and were most likely formed by magma mingling due to contact with the felsic magma and country rock. Similarly, the MME in the country rock granite porphyry also experienced a high degree of contamination by felsic magma. The MME sample HN14-1 has a SiO<sub>2</sub> content of 61.9 wt. %, again suggesting strong contamination from the host rock, and thus cannot be used for tracing the mantle source.

The rhyolitic porphyry and the granitic porphyry country rock have similar geochemical features. They have high SiO<sub>2</sub>, low MgO and Fe<sub>2</sub>O<sub>3</sub>, high Al<sub>2</sub>O<sub>3</sub>, negative Eu, Ba, U, and Sr anomalies, and negative  $\epsilon_{\text{Nd}}(t)$  values of -3.1 to -4.5, indicating an enriched continental crust source. It should also be noted that the Cretaceous igneous rocks of the Jiamusi Block have systematically higher initial <sup>87</sup>Sr/<sup>86</sup>Sr values than those in the Wandashan Orogen, indicating that the high <sup>87</sup>Sr/<sup>86</sup>Sr source was from the Jiamusi Block crust rather than subducted sediments.

In summary, magmatism in the Jiamusi block was bimodal, characterized by the volcanic strata, composite dikes, and MMEs. The andesitic rocks are minor and were formed by magma mingling, especially when mafic and felsic magmas injected into the same fracture or where mafic magma was injected into an felsic magma chamber. This bimodal signature suggests strong tectonic extension and asthenosphere upwelling related to slab rollback.

## 6.2. Arc Migration Over Time

Our study strengthens the models arguing for eastward migration of back-arc magmatism during the Cretaceous, triggered by Paleo-Pacific subduction and rollback (see Sun et al., 2013). Recent publications on Cretaceous magmatism in the Sikhote-Alin arc also discuss the spatial and temporal distribution of igneous rocks (Jahn et al., 2015; Zhao et al., 2017). These igneous rocks, from Jiamusi to Sikhote-Alin, have isotopic similarities as shown in the two-stage Nd model age (TDM2) distribution diagram (Figure 8b). A compilation of published magmatic ages shows that the Cretaceous Sikhote-Alin arc rocks also have an eastward migration trend, complementary to the migration of the back-arc magmatism (Figures 10a and 10b). Early Cretaceous magmatism primarily occurred in the western Sikhote-Alin, whereas Late Cretaceous magmatism mainly occurred in the eastern Sikhote-Alin.

A compilation of the key features of the Songliao-Jiamusi back arc and the Sikhote-Alin arc is summarized in Table 1. The contrasting styles of magmatism and tectonics clearly show that the two regions should be viewed as an arc and back-arc system migrating over time.

The onset of arc magmatism is fundamental for understanding the tectonic framework. The oldest granite (~130 Ma), as shown in the age distribution map, provides a constraint to the early stage of the magmatic arc. However, the initiation of this magmatic arc could tentatively extend as far



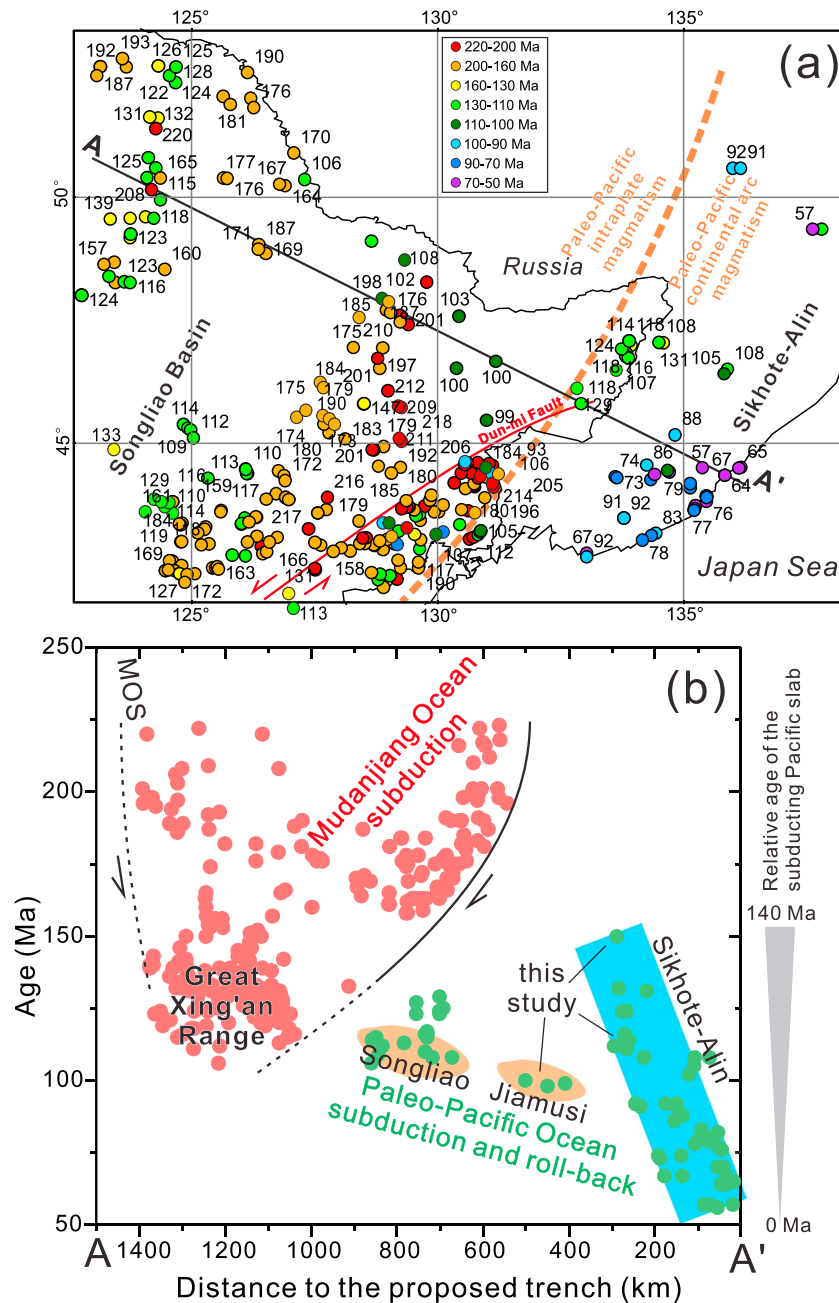


**Figure 10.** Eastern NE China and Russian Primorye igneous rock ages: (a) Spatial distribution and (b) timescale plot as projected onto the cross section (modified from Sun et al., 2013, by adding the age data from Jahn et al., 2015; Qin et al., 2016; Tang et al., 2016; Wu et al., 2011; Xu et al., 2013; Yu et al., 2012; Zhao et al., 2017). The MOS in (b) is Mongol-Okhotsk Ocean subduction. The ages of igneous rocks in the Khanka Block to the south of the Dun-mi Fault shown in (a) are not plotted on (b) because strike-slip fault movement caused the block to be displaced several hundred kilometers away from its original location.

back as ~150 Ma. This is based on (1) significant populations of ~150 Ma zircon xenocrysts in the lamprophyre, which could be sourced from a *blind* pluton at depth, and (2) the ~150 Ma youngest group of detrital zircons from the trench-slope deposit (Sun et al., 2015). The xenocrystic zircon age spectra in the Hamahe pluton are mostly between ~150 and ~120 Ma suggestive of magmatic populations, with only scattered ages (<15%) with peaks at ~160, ~260, ~480, and ~683 Ma (Figure 5d). The initiation did not likely occur earlier because the accreted intraoceanic rocks and the earliest trench-slope deposits intruded by the arc plutons formed in the mid-Jurassic and latest Jurassic (Sun et al., 2015).

**Table 1**  
*Cretaceous Magmatism in NE China and Russian Far East and Tectonic Discrimination*

	Songliao-Jiamusi	Sikhote-Alin
<b>Location</b>	Intraplate	Continental margin
<b>Basement rocks</b>	Mature continental crust	Immature continental crust
<b>Spatial and temporal distribution</b>	Proterozoic-Cambrian igneous and metamorphic rocks Stage 1 (~130 to ~90 Ma): temporal eastward migration with a rate of 1.8 cm/yr Stage 2 (~90 to ~65 Ma): magmatic lull	Late Paleozoic-Mesozoic accretionary complex Eastward migration since latest Jurassic with a rate of 0.5 cm/yr (~150 to 65 Ma)
<b>Distinguishing rock association</b>	Stage 1: bimodal magmatism including basalt, Ferroan rhyolite, I- and A-type granites; Stage 2: OIB-type basalt	Intermediate-acidic rocks including high-Mg andesite, adakite, I- and S-type granites
<b>Magma series</b>	Tholeiitic to alkaline series	Calc-alkaline series
<b>Geochemical signature</b>	Stage 1: arc-type Stage 2: OIB-type	Arc-type
<b>Mantle source</b>	Asthenosphere	Metasomatic mantle wedge and enriched lithospheric mantle
<b>Eruption style</b>	Mainly fissure type	Mainly central type
<b>Topographical features during eruption</b>	Usually negative, interlayered with sedimentary deposit	Usually positive, commonly not associated with basins
<b>Mechanics</b>	Stage 1: Extension Stage 2: Compression	Compression
<b>Tectonic discrimination</b>	Back arc	Continental arc

Earlier studies linked the magmatism in the Great Xing'an Range to the west of the Songliao Block with the Paleo-Pacific subduction and rollback (e.g., Sun et al., 2013; Zhang et al., 2011). However, the rollback of the slab subducting along the eastern margin of the Jiamusi Block cannot be responsible for the intraplate magmatism in the Great Xing'an Range because the arc initiated at ~150 Ma, whereas the magmatism in the Great Xing'an Range was already active since the Late Triassic. Therefore, the Jurassic to earlier Cretaceous magmatism in the Great Xing'an Range was possibly triggered by the westward subduction of the Mudanjiang Ocean, which was between the Jiamusi and Songliao blocks, and the southeastward subduction of the Mongol-Okhotsk Ocean. The above tectonic process potentially explains why there is no Cretaceous igneous belt like the Great Xing'an Range in the similar intraplate area of South China and North China, which also experienced Paleo-Pacific subduction.

### 6.3. Toward a Unified Tectonic Model for the Late Mesozoic Evolution of NE Asia

Based on our new geological observations, geochronological and geochemical data, and combined with previous research, we can summarize the tectonic history of the continental margin of Northeast China in the Late Mesozoic (Figure 11). The earliest known subduction in the NW Paleo-Pacific occurred in Late Carboniferous to Early Permian times (Bi et al., 2016; Li & Li, 2007; Sun et al., 2015), whereas the continental arc of East Asia has been formed since the Early Jurassic (Guo et al., 2015; Kim et al., 2015; Li et al., 2018; Yu et al., 2012).

In the Early to mid-Jurassic at ~180 Ma, a north-south trending continental arc occurred along the eastern margin of the Songliao Block, forming the Eastern Songliao arc (Figure 11; same as ZGC-LX Range igneous belt of Guo et al., 2015, Wang et al., 2017, and Yu et al., 2012). The Heilongjiang Complex, composed of meta-basaltic blueschists of MORB and OIB affinity (Wu et al., 2007; Zhou et al., 2010), represents westward oceanic subduction beneath the Songliao Block. The attribution of this subducted ocean plate is still in debate. It is possibly part of the Paleo-Pacific (Qin et al., 2016; Zhou et al., 2009), which means that the Jiamusi Block to the east is an allochthonous terrane. The ocean is also possibly a newly opened small ocean basin formed by Permian intraplate extension, named the Mudanjiang Ocean (Ge et al., 2017) or Heilongjiang Ocean (Zhu et al., 2017). If this is correct, then the Jiamusi Block was unified with the Songliao Block before the late Paleozoic, supported by the evidence that both blocks have a Pan-African metamorphic record (Zhou et al., 2011). It should be emphasized that the Mudanjiang mid-oceanic ridge was unlikely to be still spreading as late as ~142 Ma (Zhu et al., 2015) because continental arc magmatism in the ZGC-LX Range igneous belt ceased in the Late Jurassic. Compelling evidence of Jurassic magmatism and associated sedimentary records on the Jiamusi Block is lacking, which we argue is indicative of passive margins bounding the Jiamusi microcontinent. Hence, models calling for double-sided subduction of the Mudanjiang Ocean (Dong et al., 2017) appear

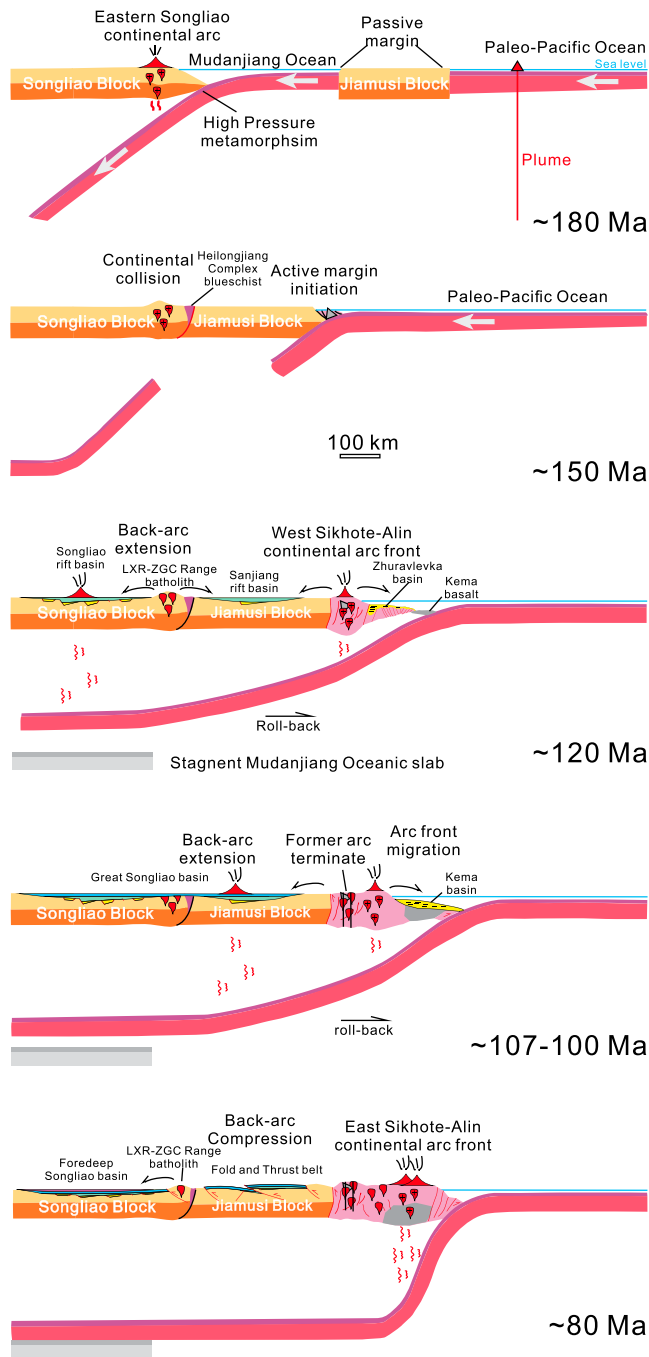


**Figure 11.** Proposed tectonic evolution model interpreting the magmatism migration trends. Synthesized and improved based on Sun et al. (2013) and Sun et al. (2015) by emphasizing the location of the arc front and its migration and also the role of the Mudanjiang Ocean.

unlikely to be correct. In the same period, oceanic islands occurred within Paleo-Pacific Ocean, triggered by mantle plume activities (Ichiyama et al., 2014; Safonova & Santosh, 2014), which laterally accreted to the eastern margin of the Jiamusi Block in the earliest Cretaceous.

In the latest Jurassic to earliest Cretaceous from ~150 Ma, the Songliao and the Jiamusi blocks collided following the closure of the Mudanjiang Ocean, causing exhumation of the Heilongjiang blueschists and the erosion of the continental arc volcanic rocks. Subduction then moved eastward to the eastern margin of the Jiamusi Block. The record of this collisional event is still weak. The  $145 \pm 1$  Ma  $^{40}\text{Ar}$ - $^{39}\text{Ar}$  age of muscovite in the Heilongjiang Complex (Li et al., 2009) possibly provides an exhumation and cooling time for this collisional event. The mid-Jurassic oceanic islands, combined with Triassic-Jurassic intraoceanic sedimentary rocks, accreted to the east margin of the Jiamusi Block and formed the embryonic Western Sikhote-Alin-Wandashan and what is now SW Japan (Kojima, 1989; Wakita, 2012).

In the Early Cretaceous at ~120 Ma, the Paleo-Pacific plate slab had reached the deep asthenosphere beneath the western edge of the Songliao Block, assuming an average convergence rate of ~5 cm/yr since 150 Ma (Seton et al., 2012). We suggest that the volcanic front flared up in the West-Sikhote-Alin (to Wandashan) Orogen represented by the Pikeshan volcanics and associated granites that extended to the Russian Samarka (Kruk et al., 2014). This magmatism followed a magmatic lull spanning ~150–120 Ma (Spencer et al., 2018). A wide variety of arc-related igneous rocks formed, for example, adakite in SW Japan and west Sikhote-Alin (Tsuchiya et al., 2007; Wu et al., 2017). We propose that the Zhuravlevka Basin was a fore-arc basin lying to the east of this continental arc and that the Kema-Moneron basalts (Malinovsky et al., 2008; Simanenko et al., 2011) further to the east formed by fore-arc volcanism related to plate rollback. In the interior of the plate, large-scale crustal extension developed, creating the Songliao and Sanjiang rift basins. Sediments sourced from the exhumation and denudation of the ZGC-LX Range were deposited into the rift basins. Simultaneous volcanic activity in the Songliao Basin formed the Yingcheng Formation A-type rhyolite (Zhang et al., 2011), marking a likely axis for this intraplate extension.

By the late Early Cretaceous (~107–100 Ma), in the back-arc region, the former continental arc ceased, resulting in the subsequent emplacement of the lamprophyre and low-HREE felsic dikes. The eastward migration of the arc front destroyed the previous Zhuravlevka fore-arc basin, and the new Kema River fore-arc basin formed, covering the Kema basalt (Malinovsky et al., 2005). Intraplate magmatism in the Songliao Basin ceased. Bimodal magmatism and composite dikes developed in the Jiamusi Block, marking the eastward migration of the extensional center. Continued erosion and subsidence eventually caused the LX-ZGC range to be submerged under water, and the Jurassic plutons ceased to be a source of sediments to the basins on both sides (Sun et al., 2014).

During the Late Cretaceous at ~80 Ma, Paleo-Pacific slab rollback continued, further migrating the continental arc eastward. The continental arc flared up again along the continental margin, forming voluminous volcanic rocks, including ignimbrites and granitoids in the East Sikhote-Alin (Grebennikov et al., 2016; Grebennikov & Popov, 2014).

In summary, we suggest that the subduction of the Paleo-Pacific plate beneath eastern NE China in the Cretaceous formed a continuously evolving continental arc and that the volcanic front did not leave the

continental margin. Moreover, old oceanic crust with an age of over 100 Ma, which had enough time for the deposition of sediments and development of seamounts, can transfer water into the mantle below the continental interior and cause intraplate extension by subduction and rollback, forming the western Pacific-type margin. Subduction of young oceanic crust with an age of less than 40 Ma tends to form an Andean-type continental margin, producing continental arc along the margin and compression in the intraplate. The global tectonic reconstruction model of Seton et al. (2012) suggests that the relative slab age of the Paleo-Pacific plate subducting at the eastern Asian continental margin in the Cretaceous decreased from ~140 to ~10 Ma. This significant decrease in age is likely to explain the transition from Early Cretaceous intraplate extension to Late Cretaceous compression in NE China.

## 7. Conclusions

Based on field geology, geochronological and geochemical studies on the Cretaceous Jiamusi-Wandashan igneous rocks, combined with the spatial and temporal distribution of Cretaceous igneous rocks in NE China and the Sikhote-Alin Orogenic Belt, we can draw the following conclusions:

1. Continental arc magmatism in the Wandashan Orogen was initiated in the earliest Cretaceous and active in the Aptian at ~118 Ma. It is characterized by intermediate-felsic rocks derived from the mantle wedge, with partial melting of the crust formed by accretion of sediments that experienced complex magma mixing and fractionation.
2. The Albian ~107-Ma intermediate lamprophyre dikes within granites of similar age mark the termination of the former continental arc and its eastward migration. This transition is recorded by calc-alkaline and alkaline lamprophyres that were derived from the metasomatized lithospheric mantle. The felsic dike with ultradepletion of HREE was from partial melting of thickened arc crust.
3. Mid-Cretaceous magmatism in the Jiamusi Block has bimodal signatures. The intermediate rocks are minor and formed by magma mingling or fractionation, indicating back-arc extension during rollback of the Paleo-Pacific slab.
4. The continental arc along the eastern NE China margin was continuously active during the Cretaceous. In the Early Cretaceous, subduction triggered intensive intraplate extension and marginal accretion by subduction of old and thick sediments covering the slab. In the Late Cretaceous, the continental arc migrated eastward and triggered retro-arc compression causing exhumation of the previous arc. Because the subducted slab was getting younger, the accretion process weakened, and a typical Cordilleran continental margin was formed.

## Acknowledgments

We thank Yang Shufeng, Dong Chuanwan, Zhang Kefeng, and Chen Dongxu for their help in the fieldtrip and Yizhuo Sun, Xinyu Wang, Shengling Sun, Xianglin Tu, and Le Zhang for geochronological and geochemical analyses. Luke Milan acknowledges support from facilities provided by the University of New England. Thanks to the Editor and Associate Editor and two anonymous reviewers for their significant contribution to the final form of the manuscript. This work was supported by the Strategic Priority Research Program (B) of Chinese Academy of Sciences (grant XDB18000000), the State Ocean Administration National Programme on Global Change and Air-Sea Interaction (grant GASI-GEOGE-02), and the National Science Foundation of China (grant 41502194). Detailed information describing data and photomicrograph are presented as supporting information. Data and photomicrograph are available as supporting information.

## References

- Bazhenov, M. L., Zharov, A. E., Levashova, N. M., Kodama, K., Bragin, N. Y., Fedorov, P. I., et al. (2001). Paleomagnetism of a Late Cretaceous island arc complex from South Sakhalin, East Asia: Convergent boundaries far away from the Asian continental margin? *Journal of Geophysical Research*, *106*(B9), 19,193–19,205. <https://doi.org/10.1029/2000JB900458>
- Bi, J. H., Ge, W. C., Yang, H., Wang, Z. H., Xu, W. L., Yang, J. H., et al. (2016). Geochronology and geochemistry of late Carboniferous–middle Permian I- and A-type granites and gabbro–diorites in the eastern Jiamusi Massif, NE China: Implications for petrogenesis and tectonic setting. *Lithos*, *266*, 213–232.
- Black, L. P., Kamo, S. L., Allen, C. M., Aleinikoff, J. N., Davis, D. W., Korsch, R. J., & Foudoulis, C. (2003). TEMORA 1: A new zircon standard for Phanerozoic U–Pb geochronology. *Chemical Geology*, *200*(1–2), 155–170.
- Bryan, S. E., Constantine, A. E., Stephens, C. J., Ewart, A., Schön, R. W., & Parianos, J. (1997). Early Cretaceous volcano-sedimentary successions along the eastern Australian continental margin: Implications for the break-up of eastern Gondwana. *Earth and Planetary Science Letters*, *153*(1–2), 85–102.
- Cao, W., Lee, C. T. A., & Lackey, J. S. (2017). Episodic nature of continental arc activity since 750 Ma: A global compilation. *Earth and Planetary Science Letters*, *461*, 85–95.
- Castillo, P. R. (2012). Adakite petrogenesis. *Lithos*, *134*, 304–316.
- Cheng, R. Y., Wu, F. Y., Ge, W. C., Sun, D. Y., Liu, X. M., & Yang, J. H. (2006). Emplacement age of the Raohe Complex in eastern Heilongjiang Province and the tectonic evolution of the eastern part of Northeastern China. *Acta Petrologica Sinica*, *22*(2), 353–376.
- Chough, S. K., & Sohn, Y. K. (2010). Tectonic and sedimentary evolution of a Cretaceous continental arc–backarc system in the Korean peninsula: New view. *Earth-Science Reviews*, *101*(3–4), 225–249.
- Cushman, S. A., & Wallin, D. O. (2000). Rates and patterns of landscape change in the Central Sikhote-alin Mountains, Russian Far East. *Landscape Ecology*, *15*(7), 643–659.
- Defant, M. J., & Drummond, M. S. (1990). Derivation of some modern arc magmas by melting of young subducted lithosphere. *Nature*, *347*(6294), 662.
- Deng, J., Yang, X., Zhang, Z. F., & Santosh, M. (2015). Early Cretaceous arc volcanic suite in Cebu Island, Central Philippines and its implications on paleo-Pacific plate subduction: Constraints from geochemistry, zircon U–Pb geochronology and Lu–Hf isotopes. *Lithos*, *230*, 166–179.
- Dong, Y., Ge, W. C., Yang, H., Ji, Z., He, Y., Zhao, D., & Xu, W. (2018). Convergence history of the Jiamusi and Songnen-Zhangguangcai range massifs: Insights from detrital zircon U Pb geochronology of the Yilan Heilongjiang complex, NE China. *Gondwana Research*.



- Dong, Y., Ge, W., Yang, H., Bi, J., Wang, Z., & Xu, W. (2017). Permian tectonic evolution of the mudanjiang ocean: Evidence from zircon U-Pb-Hf isotopes and geochemistry of a N-S trending granitoid belt in the Jiamusi Massif, NE China. *Gondwana Research*, 49, 147–163.
- Ewart, A., Schon, R. W., & Chappell, B. W. (1992). The Cretaceous volcanic-plutonic province of the central Queensland (Australia) coast—A rift related “calc-alkaline” province. *Earth and Environmental Science Transactions of the Royal Society of Edinburgh*, 83(1–2), 327–345.
- Feng, Z. Q., Jia, C. Z., Xie, X. N., Zhang, S., Feng, Z. H., & Cross, T. A. (2010). Tectonostratigraphic units and stratigraphic sequences of the nonmarine Songliao basin, northeast China. *Basin Research*, 22(1), 79–95.
- Filippov, A. N., & Kemkin, I. V. (2005). First finds of Middle Jurassic and Early Cretaceous (Valanginian) radiolarian assemblages in the Western Sikhote-Alin: Their paleogeographic and tectonic significance. *Doklady Earth Sciences*, 405(8), 1141–1144.
- Frost, C. D., & Frost, B. R. (2010). On ferroan (A-type) granitoids: Their compositional variability and modes of origin. *Journal of Petrology*, 52(1), 39–53.
- Garver, J. I., Soloviev, A. V., Bullen, M. E., & Brandon, M. T. (2000). Towards a more complete record of magmatism and exhumation in continental arcs, using detrital fission-track thermochrometry. *Physics and Chemistry of the Earth, Part A: Solid Earth and Geodesy*, 25(6–7), 565–570.
- Ge, M. H., Zhang, J. J., Li, L., Liu, K., Ling, Y. Y., Wang, J. M., & Wang, M. (2017). Geochronology and geochemistry of the Heilongjiang Complex and the granitoids from the Lesser Xing’an-Zhangguangcai Range: Implications for the late Paleozoic-Mesozoic tectonics of eastern NE China. *Tectonophysics*, 717, 565–584.
- Gill, R. (2010). *Igneous rocks and processes: A practical guide*. New York: John Wiley.
- Grebennikov, A. V., Khanchuk, A. I., Gonevchuk, V. G., & Kovalenko, S. V. (2016). Cretaceous and Paleogene granitoid suites of the Sikhote-Alin area (Far East Russia): Geochemistry and tectonic implications. *Lithos*, 261, 250–261.
- Grebennikov, A. V., & Popov, V. K. (2014). Petrogeochemical aspects of the Late Cretaceous and Paleogene ignimbrite volcanism of East Sikhote-Alin. *Russian Journal of Pacific Geology*, 8(1), 38–55.
- Guo, F., Li, H., Fan, W., Li, J., Zhao, L., Huang, M., & Xu, W. (2015). Early Jurassic subduction of the Paleo-Pacific Ocean in NE China: Petrologic and geochemical evidence from the Tumen mafic intrusive complex. *Lithos*, 224, 46–60.
- Huang, C. K., & Li H. C. (2001). 1:500 000 digital geological maps and spatial metadata of People’s Republic of China (in Chinese). *Chinese Geology*, 28, 2.
- Ichiyama, Y., Ishiwatari, A., Kimura, J. I., Senda, R., & Miyamoto, T. (2014). Jurassic plume-origin ophiolites in Japan: Accreted fragments of oceanic plateaus. *Contributions to Mineralogy and Petrology*, 168(1), 1019.
- Imaoka, T., Kawabata, H., Nagashima, M., Nakashima, K., Kamei, A., Yagi, K., et al. (2017). Petrogenesis of an early cretaceous lamprophyre dike from Kyoto Prefecture, Japan: Implications for the generation of high-Nb basalt magmas in subduction zones. *Lithos*, 290–291, 18–33.
- Jahn, B. M., Valui, G., Kruk, N., Gonevchuk, V., Usuki, M., & Wu, J. T. (2015). Emplacement ages, geochemical and Sr-Nd-Hf isotopic characterization of Mesozoic to early Cenozoic granitoids of the Sikhote-Alin Orogenic Belt, Russian Far East: Crustal growth and regional tectonic evolution. *Journal of Asian Earth Sciences*, 111, 872–918.
- Jiang, H., & Lee, C. T. A. (2017). Coupled magmatism–erosion in continental arcs: Reconstructing the history of the Cretaceous Peninsular Ranges batholith, southern California through detrital hornblende barometry in forearc sediments. *Earth and Planetary Science Letters*, 472, 69–81.
- Jourdan, F., & Renne, P. R. (2007). Age calibration of the Fish Canyon sanidine  $^{40}\text{Ar}/^{39}\text{Ar}$  dating standard using primary K–Ar standards. *Geochimica et Cosmochimica Acta*, 71(2), 387–402.
- Katzir, Y., Litvinovsky, B. A., Jahn, B. M., Eyal, M., Zandvilevich, A. N., Valley, J. W., et al. (2007). Interrelations between coeval mafic and A-type silicic magmas from composite dykes in a bimodal suite of southern Israel, northernmost Arabian–Nubian Shield: Geochemical and isotope constraints. *Lithos*, 97(3), 336–364.
- Kelemen, P. B. (1995). Genesis of high Mg# andesites and the continental crust. *Contributions to Mineralogy and Petrology*, 120(1), 1–19.
- Khanchuk, A. I., Kemkin, I. V., & Kruk, N. N. (2016). The Sikhote-Alin orogenic belt, Russian South East: Terranes and the formation of continental lithosphere based on geological and isotopic data. *Journal of Asian Earth Sciences*, 120, 117–138.
- Kim, S. W., Kwon, S., Ko, K., Yi, K., Cho, D. L., Kee, W. S., & Kim, B. C. (2015). Geochronological and geochemical implications of Early to Middle Jurassic continental adakitic arc magmatism in the Korean Peninsula. *Lithos*, 227, 225–240.
- Kirsch, M., Paterson, S. R., Wobbe, F., Ardila, A. M. M., Clausen, B. L., & Alasino, P. H. (2016). Temporal histories of Cordilleran continental arcs: Testing models for magmatic episodicity. *American Mineralogist*, 101(10), 2133–2154.
- Kojima, S. (1989). Mesozoic terrane accretion in northeast China, Sikhote-Alin and Japan regions. *Palaeogeography, Palaeoclimatology, Palaeoecology*, 69, 213–232.
- Kolb, M., von Quadt, A., Peytcheva, I., Heinrich, C. A., Fowler, S. J., & Cvetković, V. (2012). Adakite-like and normal arc magmas: Distinct fractionation paths in the East Serbian segment of the Balkan–Carpathian arc. *Journal of Petrology*, 54(3), 421–451.
- Koppers, A. A. (2002). ArArCALC—Software for  $^{40}\text{Ar}/^{39}\text{Ar}$  age calculations. *Computers & Geosciences*, 28(5), 605–619.
- Kruk, N. N., Simanenkov, V. P., Gvozdev, V. I., Golozubov, V. V., Kovach, V. P., Serov, P. I., et al. (2014). Early Cretaceous granitoids of the Samarka terrane (Sikhote-Alin): Geochemistry and sources of melts. *Russian Geology and Geophysics*, 55(2), 216–236.
- Lee, C. T. A., Thurner, S., Paterson, S., & Cao, W. (2015). The rise and fall of continental arcs: Interplays between magmatism, uplift, weathering, and climate. *Earth and Planetary Science Letters*, 425, 105–119.
- Lee, J. Y., Marti, K., Severinghaus, J. P., Kawamura, K., Yoo, H. S., Lee, J. B., & Kim, J. S. (2006). A redetermination of the isotopic abundances of atmospheric Ar. *Geochimica et Cosmochimica Acta*, 70(17), 4507–4512.
- Li, J., Dong, S., Cawood, P. A., Zhao, G., Johnston, S. T., Zhang, Y., & Xin, Y. (2018). An Andean-type retro-arc foreland system beneath northwest South China revealed by SINOProbe profiling. *Earth and Planetary Science Letters*, 490, 170–179.
- Li, W., Takasu, A., Liu, Y., Genser, J., Neubauer, F., & Guo, X. (2009).  $^{40}\text{Ar}/^{39}\text{Ar}$  ages of the high-P/T metamorphic rocks of the Heilongjiang Complex in the Jiamusi Massif, northeastern China. *Journal of Mineralogical and Petrological Sciences*, 104(2), 110–116.
- Li, Z. X., & Li, X. H. (2007). Formation of the 1300-km-wide intracontinental orogen and postorogenic magmatic province in Mesozoic South China: A flat-slab subduction model. *Geology*, 35(2), 179–182.
- Liu, K., Zhang, J., Wilde, S. A., Liu, S., Guo, F., Kasatkin, S. A., et al. (2017). U-Pb dating and Lu-Hf isotopes of detrital zircons from the Southern Sikhote-Alin Orogenic Belt, Russian Far East: Tectonic implications for the Early Cretaceous evolution of the Northwest Pacific Margin. *Tectonics*, 36, 2555–2598. <https://doi.org/10.1002/2017TC004599>
- Ludwig, K. R. (2001). SQUID 1.02: A user’s manual. Berkeley, CA: Berkeley Geochronological Center.
- Ludwig, K. R. (2003). User’s manual for Isoplot 3.00: A geochronological toolkit for Microsoft Excel. *Berkeley Geochronology Center, Special Publication*, 4, 25–32.
- Malinovsky, A. I., Golozubov, V. V., Simanenkov, V. P., & Simanenkov, L. F. (2008). Kema terrane: A fragment of a back-arc basin of the early Cretaceous Moneron–Samarga island-arc system, East Sikhote–Alin range, Russian Far East. *Island Arc*, 17(3), 285–304.

- Malinovsky, A. I., Golozubov, V. V., & Simanenko, V. P. (2005). Composition and depositional settings of Lower Cretaceous terrigenous rocks of the Kema River Basin, eastern Sikhote Alin. *Lithology and Mineral Resources*, 40(5), 429–447.
- Markevich, P. V., Malinovsky, A. I., Tuchkova, M. I., Sokolov, S. D., & Grigoryev, V. N. (2007). The use of heavy minerals in determining the provenance and tectonic evolution of Mesozoic and Cenozoic sedimentary basins in the continent-Pacific Ocean transition zone: Examples from Sikhote-Alin and Koryak-Kamchatka regions (Russian Far East) and Western Pacific. *Developments in Sedimentology*, 58, 789–822.
- McDonough, W. F., & Sun, S. S. (1995). The composition of the Earth. *Chemical Geology*, 120(3–4), 223–253.
- McKenzie, N. R., Horton, B. K., Loomis, S. E., Stockli, D. F., Planavsky, N. J., & Lee, C. T. A. (2016). Continental arc volcanism as the principal driver of icehouse-greenhouse variability. *Science*, 352(6284), 444–447.
- Metcalfe, I. (2009). Late Palaeozoic and Mesozoic tectonic and palaeogeographical evolution of SE Asia. *Geological Society, London, Special Publications*, 315(1), 7–23.
- Milan, L. A., Daczko, N. R., & Clarke, G. L. (2017). Cordillera Zealandia: A Mesozoic arc flare-up on the palaeo-Pacific Gondwana Margin. *Scientific Reports*, 7(1), 261.
- Milan, L. A., Daczko, N. R., Clarke, G. L., & Allibone, A. H. (2016). Complexity of In-situ zircon U–Pb–Hf isotope systematics during arc magma genesis at the roots of a Cretaceous arc, Fiordland, New Zealand. *Lithos*, 264, 296–314.
- Pan, S., Zheng, J., Griffin, W. L., Chu, L., Xu, Y., Li, Y., et al. (2014). Precambrian tectonic attribution and evolution of the Songliao terrane revealed by zircon xenocrysts from Cenozoic alkali basalts, Xilinhot region, NE China. *Precambrian Research*, 251, 33–48.
- Paterson, S. R., Miller, R. B., Alsleben, H., Whitney, D. L., Valley, P. M., & Hurlow, H. (2004). Driving mechanisms for > 40 km of exhumation during contraction and extension in a continental arc, Cascades core, Washington. *Tectonics*, 23, TC3005. <https://doi.org/10.1029/2002TC001440>
- Pearson, D. M., MacLeod, D. R., Ducea, M. N., Gehrels, G. E., & Jonathan Patchett, P. (2017). Sediment underthrusting within a continental magmatic arc: Coast Mountains batholith, British Columbia. *Tectonics*, 36, 2022–2043. <https://doi.org/10.1002/2017TC004594>
- Perrig, C. S., & Rock, N. M. (1991). Relationships between calc-alkaline acidic and basic (mantle-derived) magmas in late Archaean composite dykes, Kambalda Goldfield, Western Australia. *Precambrian Research*, 52(3–4), 245–273.
- Qin, J. F., Lai, S. C., Li, Y. F., Ju, Y. J., Zhu, R. Z., & Zhao, S. W. (2016). Early Jurassic monzogranite-tonalite association from the southern Zhangguangcai Range: Implications for paleo-Pacific plate subduction along northeastern China. *Lithosphere*, 8(4), 396–411.
- Renne, P. R., Balco, G., Ludwig, K. R., Mundil, R., & Min, K. (2011). Response to the comment by WH Schwarz et al. on “Joint determination of 40K decay constants and  $^{40}\text{Ar}^*/^{40}\text{K}$  for the Fish Canyon sanidine standard, and improved accuracy for  $^{40}\text{Ar}/^{39}\text{Ar}$  geochronology” by PR Renne et al. (2010). *Geochimica et Cosmochimica Acta*, 75(17), 5,097–5,100.
- Renne, P. R., Deino, A. L., Hilgen, F. J., Kuiper, K. F., Mark, D. F., Mitchell, W. S., et al. (2013). Time scales of critical events around the Cretaceous-Paleogene boundary. *Science*, 339(6120), 684–687.
- Renne, P. R., Mundil, R., Balco, G., Min, K., & Ludwig, K. R. (2010). Joint determination of 40K decay constants and  $^{40}\text{Ar}^*/^{40}\text{K}$  for the Fish Canyon sanidine standard, and improved accuracy for  $^{40}\text{Ar}/^{39}\text{Ar}$  geochronology. *Geochimica et Cosmochimica Acta*, 74(18), 5349–5367.
- Rey, P. F. (2013). Opalisation of the Great Artesian Basin (central Australia): An Australian story with a Martian twist. *Australian Journal of Earth Sciences*, 60(3), 291–314.
- Safonova, I. Y., & Santosh, M. (2014). Accretionary complexes in the Asia-Pacific region: Tracing archives of ocean plate stratigraphy and tracking mantle plumes. *Gondwana Research*, 25(1), 126–158.
- Seton, M., Müller, R. D., Zahirovic, S., Gaina, C., Torsvik, T., Shephard, G., et al. (2012). Global continental and ocean basin reconstructions since 200 Ma. *Earth-Science Reviews*, 113(3–4), 212–270.
- Simanenko, V. P., Rasskazov, S. V., Yasnygina, T. A., Simanenko, L. F., & Chashchin, A. A. (2011). Cretaceous complexes of the frontal zone of the Moneron-Samarga Island arc: Geochemical data on the basalts from the deep borehole on Moneron Island, the Sea of Japan. *Russian Journal of Pacific Geology*, 5(1), 26–46.
- Snyder, D., Crambes, C., Tait, S., & Wiebe, R. A. (1997). Magma mingling in dikes and sills. *The Journal of Geology*, 105(1), 75–86.
- Spencer, C. J., Murphy, J. B., Kirkland, C. L., Liu, Y., & Mitchell, R. N. (2018). A Palaeoproterozoic tectono-magmatic lull as a potential trigger for the supercontinent cycle. *Nature Geoscience*, 11, 97–101.
- Stern, R. A. (2001). A new isotopic and trace-element standard for the ion microprobe: preliminary thermal ionization mass spectrometry (TIMS) U-Pb and electron-microprobe data. *Ressources Naturelles Canada*.
- Stern, R. J., & Voegeli, D. A. (1987). Geochemistry, geochronology, and petrogenesis of a Late Precambrian (~ 590 Ma) composite dike from the North Eastern Desert of Egypt. *Geologische Rundschau*, 76(2), 325–341.
- Sun, M., Chen, H., Zhang, F., Wilde, S. A., Minna, A., Lin, X., & Yang, S. (2014). Cretaceous provenance change in the Hegang Basin and its connection with the Songliao Basin, NE China: Evidence for lithospheric extension driven by palaeo-Pacific roll-back. *Geological Society, London, Special Publications*, 413, 91–117.
- Sun, M. D., Chen, H. L., Zhang, F. Q., Wilde, S. A., Dong, C. W., & Yang, S. F. (2013). A 100 Ma bimodal composite dyke complex in the Jiamusi Block, NE China: An indication for lithospheric extension driven by Paleo-Pacific roll-back. *Lithos*, 162, 317–330.
- Sun, M. D., Xu, Y. G., Wilde, S. A., & Chen, H. L. (2015). Provenance of Cretaceous trench slope sediments from the Mesozoic Wandashan Orogen, NE China: Implications for determining ancient drainage systems and tectonics of the Paleo-Pacific. *Tectonics*, 34, 1269–1289. <https://doi.org/10.1002/2015TC003870>
- Tang, J., Xu, W., Niu, Y., Wang, F., Ge, W., Sorokin, A. A., & Chekryzhov, I. Y. (2016). Geochronology and geochemistry of Late Cretaceous–Paleocene granitoids in the Sikhote-Alin Orogenic Belt: Petrogenesis and implications for the oblique subduction of the paleo-Pacific plate. *Lithos*, 266, 202–212.
- Tang, M., Erdman, M., Eldridge, G., & Lee, C. T. A. (2018). The redox “filter” beneath magmatic orogens and the formation of continental crust. *Science Advances*, 4(5), eaar4444. <https://doi.org/10.1126/sciadv.aar4444>
- Tatsumi, Y. (2001). Geochemical modeling of partial melting of subducting sediments and subsequent melt-mantle interaction: Generation of high-Mg andesites in the Setouchi volcanic belt, southwest Japan. *Geology*, 29(4), 323–326.
- Taylor, T. R., Vogel, T. A., & Wilband, J. T. (1980). The composite dikes at Mount Desert Island, Maine: An example of coexisting acidic and basic magmas. *The Journal of Geology*, 88(4), 433–444.
- Tsuchiya, N., Kimura, J. I., & Kagami, H. (2007). Petrogenesis of Early Cretaceous adakitic granites from the Kitakami mountains, Japan. *Journal of Volcanology and Geothermal Research*, 167(1–4), 134–159.
- Wakita, K. (2012). Mappable features of mélanges derived from Ocean Plate Stratigraphy in the Jurassic accretionary complexes of Mino and Chichibu terranes in Southwest Japan. *Tectonophysics*, 568, 74–85.
- Wan, Y., Li, R., Wilde, S. A., Liu, D., Chen, Z., Yan, L., et al. (2005). UHP metamorphism and exhumation of the Dabie Orogen, China: Evidence from SHRIMP dating of zircon and monazite from a UHP granitic gneiss cobble from the Hefei Basin. *Geochimica et Cosmochimica Acta*, 69(17), 4333–4348.

- Wang, F., Xu, Y. G., Xu, W. L., Yang, L., Wu, W., & Sun, C. Y. (2017). Early Jurassic calc-alkaline magmatism in northeast China: Magmatic response to subduction of the Paleo-Pacific Plate beneath the Eurasian continent. *Journal of Asian Earth Sciences*, *143*, 249–268.
- Wang, X. C., Wilde, S. A., Xu, B., & Pang, C. J. (2016). Origin of arc-like continental basalts: Implications for deep-Earth fluid cycling and tectonic discrimination. *Lithos*, *261*, 5–45.
- Wiebe, R. A., & Ulrich, R. (1997). Origin of composite dikes in the Gouldsboro granite, coastal Maine. *Lithos*, *40*(2–4), 157–178.
- Wilde, S. A., Wu, F., & Zhang, X. (2003). Late Pan-African magmatism in northeastern China: SHRIMP U–Pb zircon evidence from granitoids in the Jiamusi Massif. *Precambrian Research*, *122*(1–4), 311–327.
- Williams, I. S. (1998). U–Th–Pb geochronology by ion microprobe. *Reviews in Economic Geology*, *7*, 1–35.
- Wu, F. Y., Sun, D. Y., Ge, W. C., Zhang, Y. B., Grant, M. L., Wilde, S. A., & Jahn, B. M. (2011). Geochronology of the Phanerozoic granitoids in northeastern China. *Journal of Asian Earth Sciences*, *41*(1), 1–30.
- Wu, F. Y., Yang, J. H., Lo, C. H., Wilde, S. A., Sun, D. Y., & Jahn, B. M. (2007). The Heilongjiang Group: A Jurassic accretionary complex in the Jiamusi Massif at the western Pacific margin of northeastern China. *Island Arc*, *16*(1), 156–172.
- Wu, J. T. J., Jahn, B. M., Nechaev, V., Chashchin, A., Popov, V., Yokoyama, K., & Tsutsumi, Y. (2017). Geochemical characteristics and petrogenesis of adakites in the Sikhote-Alin area, Russian Far East. *Journal of Asian Earth Sciences*, *145*, 512–529.
- Xu, W. L., Pei, F. P., Wang, F., Meng, E., Ji, W. Q., Yang, D. B., & Wang, W. (2013). Spatial–temporal relationships of Mesozoic volcanic rocks in NE China: Constraints on tectonic overprinting and transformations between multiple tectonic regimes. *Journal of Asian Earth Sciences*, *74*, 167–197.
- Yang, H., Ge, W. C., Bi, J. H., Wang, Z. H., Tian, D. X., Dong, Y., & Chen, H. J. (2018). The Neoproterozoic–early Paleozoic evolution of the Jiamusi Block, NE China and its East Gondwana connection: Geochemical and zircon U–Pb–Hf isotopic constraints from the Mashan Complex. *Gondwana Research*, *54*, 102–121.
- Yu, J. J., Wang, F., Xu, W. L., Gao, F. H., & Pei, F. P. (2012). Early Jurassic mafic magmatism in the Lesser Xing’an–Zhangguangcai Range, NE China, and its tectonic implications: Constraints from zircon U–Pb chronology and geochemistry. *Lithos*, *142*, 256–266.
- Zhang, F. Q., Chen, H. L., Yang, S. F., Feng, Z. Q., Wu, H. Y., Batt, G. E., et al. (2012). Late Mesozoic–Cenozoic evolution of the Sanjiang Basin in NE China and its tectonic implications for the West Pacific continental margin. *Journal of Asian Earth Sciences*, *49*, 287–299.
- Zhang, F. Q., Chen, H. L., Yu, X., Dong, C. W., Yang, S. F., Pang, Y. M., & Batt, G. E. (2011). Early Cretaceous volcanism in the northern Songliao Basin, NE China, and its geodynamic implication. *Gondwana Research*, *19*(1), 163–176.
- Zhang, F. Q., Dilek, Y., Chen, H. L., Yang, S. F., & Meng, Q. A. (2017). Structural architecture and stratigraphic record of Late Mesozoic sedimentary basins in NE China: Tectonic archives of the Late Cretaceous continental margin evolution in East Asia. *Earth-Science Reviews*, *171*, 598–620.
- Zhao, P., Jahn, B. M., & Xu, B. (2017). Elemental and Sr–Nd isotopic geochemistry of Cretaceous to Early Paleogene granites and volcanic rocks in the Sikhote-Alin Orogenic Belt (Russian Far East): Implications for the regional tectonic evolution. *Journal of Asian Earth Sciences*, *146*, 383–401.
- Zhou, J. B., Wilde, S. A., Zhang, X. Z., Zhao, G. C., Liu, F. L., Qiao, D. W., et al. (2011). A > 1300 km late Pan-African metamorphic belt in NE China: New evidence from the Xing’an block and its tectonic implications. *Tectonophysics*, *509*(3–4), 280–292.
- Zhou, J. B., Wilde, S. A., Zhang, X. Z., Zhao, G. C., Zheng, C. Q., Wang, Y. J., & Zhang, X. H. (2009). The onset of Pacific margin accretion in NE China: Evidence from the Heilongjiang high-pressure metamorphic belt. *Tectonophysics*, *478*(3–4), 230–246.
- Zhou, J. B., Wilde, S. A., Zhao, G. C., Zhang, X. Z., Zheng, C. Q., & Wang, H. (2010). New SHRIMP U–Pb zircon ages from the Heilongjiang high-pressure belt: Constraints on the Mesozoic evolution of NE China. *American Journal of Science*, *310*(9), 1024–1053.
- Zhu, C. Y., Zhao, G., Ji, J., Sun, M., Han, Y., Liu, Q., et al. (2017). Subduction between the jiamusi and songliao blocks: Geological, geochronological and geochemical constraints from the heilongjiang complex. *Lithos*, *282–283*, 128–144.
- Zhu, C. Y., Zhao, G., Sun, M., Han, Y., Liu, Q., Eizenhöfer, P. R., et al. (2017). Detrital zircon U–Pb and Hf isotopic data for meta-sedimentary rocks from the Heilongjiang Complex, northeastern China and tectonic implications. *Lithos*, *282*, 23–32.